Project number 813137

URBASIS-EU
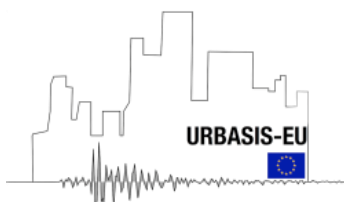New challenges for Urban Engineering Seismology

## DELIVERABLE

**Work Package: WP3**

**Number: D3.2 – A case study on non-linear soil response in urban areas**

| Authors: | **Janusz, Paulina** | (UGA) |
| Co-Authors: | Bonilla, Luis Fabian | (UGE) |
| | Fäh, Donat | (SED – ETH Zürich) |

URBASIS-EU

# A case study on non-linear soil response in urban areas

## Contents

### 1. Introduction

When assessing local seismic hazard, analysis of site effects cannot be ignored. Earthquake risk is especially high in densely populated urban areas due to the concentration of vulnerable elements such as infrastructure and high population density. Soil amplification is dependent on the amplitude of the ground motion and for strong earthquakes that relation becomes non-linear (e.g. Beresnev & Wen, 1996; Bonilla et al., 2005; Roten et al., 2009). The shear modulus decreases and the damping ratio increases with increasing strain above a certain strain threshold (Beresnev & Wen, 1996). Because of the higher damping ratio at high strain levels, the amplitude of the ground motion usually decreases especially at high frequencies. In some cases, we can observe even de-amplification, which is the reason why non-linear effects are often not considered or underestimated while assessing the seismic hazard. However, at the same time, because of the reduction of shear modulus, the shear wave velocity and fundamental frequency of the soil decrease, increasing soil amplification factors

at lower frequencies (Beresnev & Wen, 1996). Because fundamental resonance frequencies characteristic for many buildings are usually at low frequencies, non-linear site effects can significantly contribute to the damage. Moreover, expansive soils can temporarily regain their shear strength when subjected to strong vibrations, leading to large deformations (Bonilla et al., 2005). In case of a sudden increase of pore pressure under undrained conditions, soils can lose shear strength and start behaving like a fluid. Such a phenomenon is called liquefaction and is known to cause extensive damage to buildings and infrastructure (Kramer, 1996).

For analysing and predicting the effects of weak and intermediate ground motion, it is common to consider only linear soil response using observation of weak and distant earthquakes with methods such as classical Standard Spectral Ratio (SSR; Borcherdt, 1970) or methods based on Generalized Inversion Techniques (GIT; e.g. Andrews, 1986; Edwards et al., 2013). Some authors try to predict amplification by using also some proxies (e.g. Bergamo et al., 2020, 2021a; Boudghene Stambouli et al., 2017; Derras et al., 2017; Panzera, et al., 2021a) or by combining earthquake ground-motion with ambient vibration data (Janusz et al., 2021, 2022; Perron et al., 2018, 2022). More information about different methods of linear site analysis can be found in our previous report in which we summarize several methods as well as present real case studies (Janusz et al., 2021).

To analyse non-linear site response, we need observation of strong motion, preferably in vertical arrays, which are not commonly accessible in many areas, especially where strong earthquakes are experienced once in several centuries. Hence, it is common to simulate non-linear soil behaviour using either simple assumptions such as an equivalent linear model that requires only a few parameters (Schnabel et al., 1972) or sophisticated fully non-linear models (e.g. Yoshida & Iai, 1998; Yu et al., 1993). Analyzing the non-linear soil behaviour in seismological data is one of the important topics in the community of seismologists and earthquake engineers (e.g. Bonilla et al., 2019; Chandra et al., 2015, 2016; Gueguen et al., 2018; Regnier, 2021).

However, for verification of the non-linear simulations, we still need strong motion data. In our case study, in the city of Lucerne in central Switzerland, the strongest historical earthquake was in 1601 with a magnitude of 5.9 (Fäh et al., 2011). In addition, there are studies indicating stronger paleo-earthquakes in the area (Mw 6.5-7.0; Kremer et al., 2017; Strasser et al., 2006). Nevertheless, we do not know if the incident wavefield was strong enough to trigger non-linear effects. For the last 50 years, the seismicity in the area was low (Gisler et al., 2004), so no recordings are showing non-linear site effects. Moreover, there is no evidence of liquefaction in the city, even though strong deformation was found in the Lucerne lake sediments (Siegenthaler et al., 1987) indicating liquefaction possibility. However, because of very soft saturated sediments in the shallow depths of the Lucerne basin, the liquefaction hazard is relatively high; hence, we cannot neglect analysing non-linear soil behaviour, even though, we have no data to verify our results.

In this report, we will first describe the methods and models to analyse and account for non-linear soil behaviour used in this study. Then, we will show some results for the Lucerne area including calibration of geotechnical and geotechnical soil parameters using CPT data, and finding dilatancy parameters needed in the numerical model. They come from the inversion

scheme introduced by Roten, (2014) that uses the Neighborhood algorithm (Sambridge, 1999a, 1999b, 2003). Because the procedure was never tested using a real case study, we performed several experiments to exam and refine the process, analyse its performance and investigate its weaknesses. In the next step, we will present a 1D simulation of the ground motion propagation in non-linear media for a selected site including sensitivity analysis of some input parameters for example dilatancy parameters.

One of our aims in the case of the Lucerne area, where no verification data is available, is to assess the reliability of our non-linear simulations by checking if the resulting values are reasonable when compared to other areas where we observe strong motion. Our motivation here is to check how much the site response will change when using a non-linear model compared to a linear one for this specific case study where we perform a very detailed analysis. This study is also intended to provide more information about including the non-linear behaviour for assessing the seismic hazard and risk for Switzerland (Bergamo, et al., 2021b). Another aspect we want to investigate is some uncertainties involved to allow us to make any conclusions about non-linearity. We would like also to estimate how strong an earthquake should be to trigger non-linear site effects and liquefaction for our soil models using ground motions for different return periods. Last but not least, in the future, we would like to study the influence of 2D/3D resonances on site response using both linear and non-linear models. In the following report, not all of those questions will be addressed because it is still ongoing work. We will focus on the investigation of 1D non-linear response analysis and calibration of input parameters.

2. Methods for analyzing non-linear site response used in the study

One of the tools that allow performing both total and effective stress analysis is the finite-difference code NOAH (**NO**n-linear **A**nelastic **H**ysteretic - Bonilla, 2001; Bonilla et al., 2005). It simulates non-linear wave propagation in water-saturated deposits due to a vertically incident SH wave. The code implements the strain space multishear mechanism model (Towhata & Ishihara, 1985) and the liquefaction front model (Iai et al., 1990). The models describe the hysteretic behaviour of stress-strain relation and development of pore pressure excess considering also dilatancy and cyclic mobility of sands. Examples of the applications can be found in Bonilla et al., (2005), Roten et al., (2014), and Roten et al., (2009).

For linear ground motion simulations, we need a few parameters, usually compressional ($V_p$) and shear ($V_s$) wave velocity profiles, density ($\rho$), and attenuation quality factors ($Q_p$ and $Q_s$). However, for non-linear calculations, depending on the complexity of the constitutive equation (rheology), many more soil properties have to be defined such as the shear modulus, cohesion, angle of internal friction, shear moduli and damping as a function of strain if it is an equivalent model. Detailed characterization needed to perform fully non-linear modelling poses one of the greatest challenges for non-linear soil behaviour analysis. Commonly, needed parameters are inferred using field measurements, laboratory testing, estimated with empirical relations, or simply assumed. The order shows the decreasing cost. To consider the effects of pore pressure, five dilatancy parameters describing the pore pressure development under cyclic loading are needed (Iai et al., 1990). Parameter $p_1$ is responsible for the position of the liquefaction front in the initial phase of the deformation, while $p_2$ is the final phase

(Roten et al., 2014). Overall dilatancy $w_1$ describes both pore pressure development in the initial and final phases. Threshold limit $c_1$ indicates the starting point of the pore pressure build-up. If parameter $S_0$ is equal to 1, no pore pressure excess is generated while $S_0=0$ means that pore water pressure reaches the effective confining stress and liquefaction. However, because $S_0$ cannot be 0 for numerical stability, the dilatancy parameter $S_1$ is set to a small positive value to prevent it. In chapter 5.6, simulations of pore pressure development under cyclic loading using different sets of dilatancy parameters are shown to illustrate better their impact. Typically, the trial and error method is used to calibrate the dilatancy parameters (Bonilla et al., 2005; Iai et al., 1990). The triaxial test is performed on results from laboratory tests of soil samples and the best set of dilatancy parameters is found by trying to explain pore pressure development. The parameters are often calibrated sequentially using different shear stress levels (Iai et al., 1990).

The dilatancy parameters can be also calibrated using strong-motion vertical array records (Roten, 2014; Roten et al., 2014) or cone penetration test (CPT). CPT is an invasive geotechnical test where the probe is pushed vertically into the soil at a standard rate while measuring tip resistance $q_c$, sleeve friction $f_s$, and sometimes pore pressure (Liao et al., 2002; Robertson, 2009). If seismic piezocone modules are used (SCPTu) (Liao et al., 2002), the shear wave velocity profile can be derived by measuring the delay times of wave arrival excited by some devices. The CPT is commonly used for the characterization of soil geotechnical properties for construction purposes. It allows deriving among others the soil type and strength using different empirical relations (Liao et al., 2002; Robertson, 2009). In our study, we used CPT readings together with seismic geophysical measurements if available to determine soil properties required as an input for non-linear simulations with NOAH. We derive parameters for CPT using different empirical relations (Robertson and Wride, 1998) while the dilatancy parameters are calibrated using the inversion scheme developed by Roten, (2014) using the Neighbourhood algorithm (Sambridge, 1999a, 1999b, 2003). The idea of the inversion procedure is to invert the liquefaction resistance curve (LRC) generated from CPT data and simulate the stress-controlled triaxial experiment to find the set of dilatancy parameters that explain the LRC the best.

3. Case study and data

Lucerne is a middle-sized, but a densely populated city in central Switzerland (Figure 1a). It is located in the basin filled with unconsolidated Quaternary fluvio-lacustrine deposits that are prone to strong site effects and liquefaction. The infill primarily involves intermixed thin layers of sand, gravel, clay, and silt (Poggi et al., 2012b, Figure 1b). According to the Swiss Building Code classification (SIA261, 2020), which is comparable to the EC8 classification (EC8, 2004) and defined in terms of $V_{s30}$ ranges, such mainly very soft deposits are classified as D, C, and F categories (Poggi et al., 2012b, Figure 1c). Sedimentary layers are unevenly distributed across the basin. The bedrock contains clastic sedimentary rocks deposited in the subalpine Molasse basin, mainly hard sandstones, siltstones, and mudstones. The strong impedance contrast between bedrock and infill contributes to the high amplification factors. The basin shape is complex (Figure 2) because of its glacial origin indicating the importance of 2D and 3D site effects. The southern part of the area is a very narrow basin (about 4km long and

700m in the narrowest part with 150 m of sediments in the deepest part) while the northern part is more asymmetrical – a thick deposit layer (50-100 m thick) becomes gradually thinner from northeast close to the lakefront to the southwest. Shallow water table due to the vicinity of the Lucerne lake (i.e. 2–5 m) (Poggi et al., 2012b, Geoportal Kanton Luzern - https://geoportal.lu.ch) contributes strongly to the risk of liquefaction.
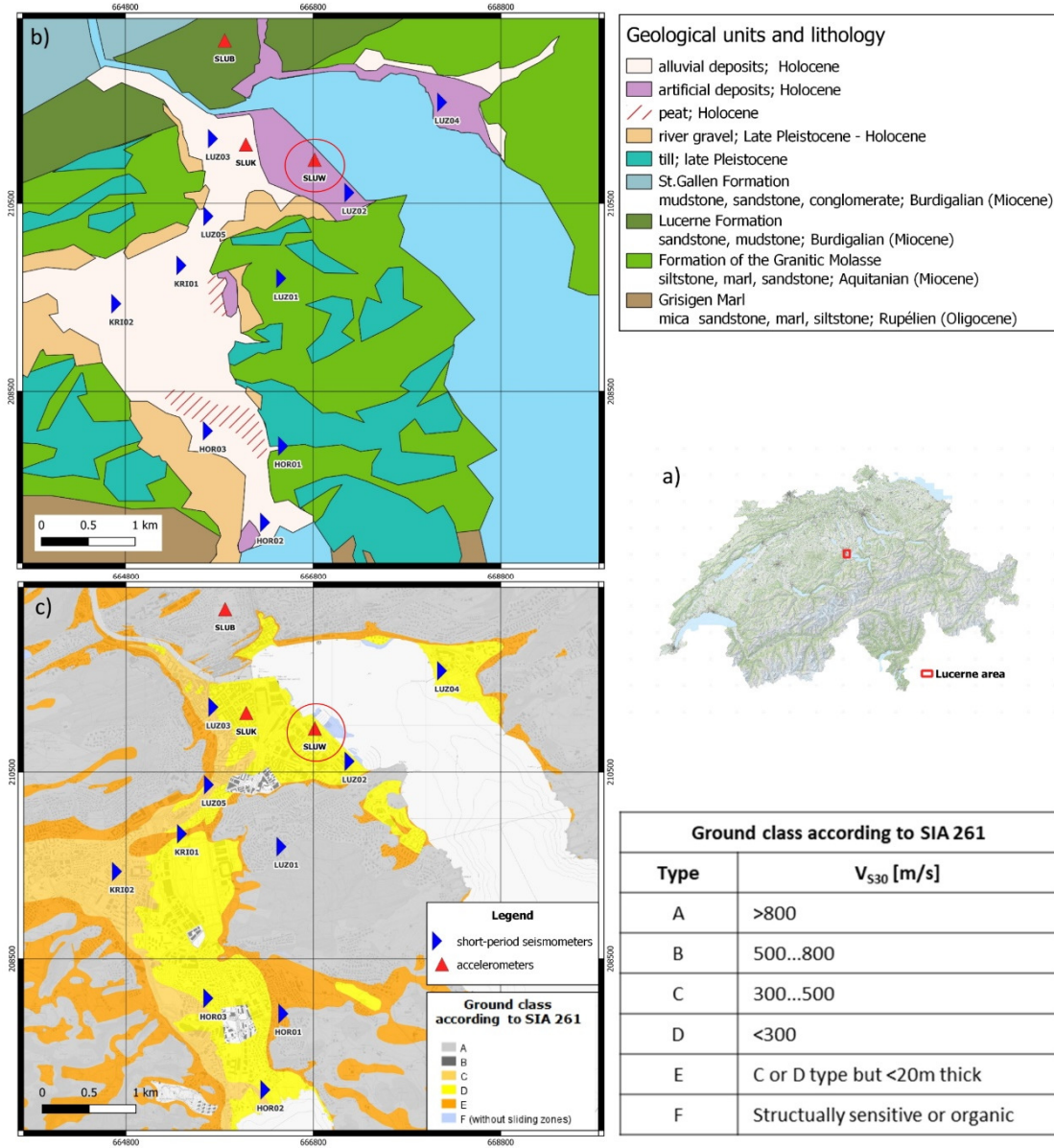


*Figure 1. a) Map of Switzerland with marked Lucerne area (red rectangular). b) Simplified geological map modified from Geological Vector Datasets GeoCover (s.geo.admin.ch/95a803e945). c) Ground classes according to SIA 261 (SIA, 2020) (s.geo.admin.ch/96572c02d9). Stations of local seismic monitoring networks are shown. Station SLUW is marked using a red circle. Figure modified from Janusz et al., (2022).*
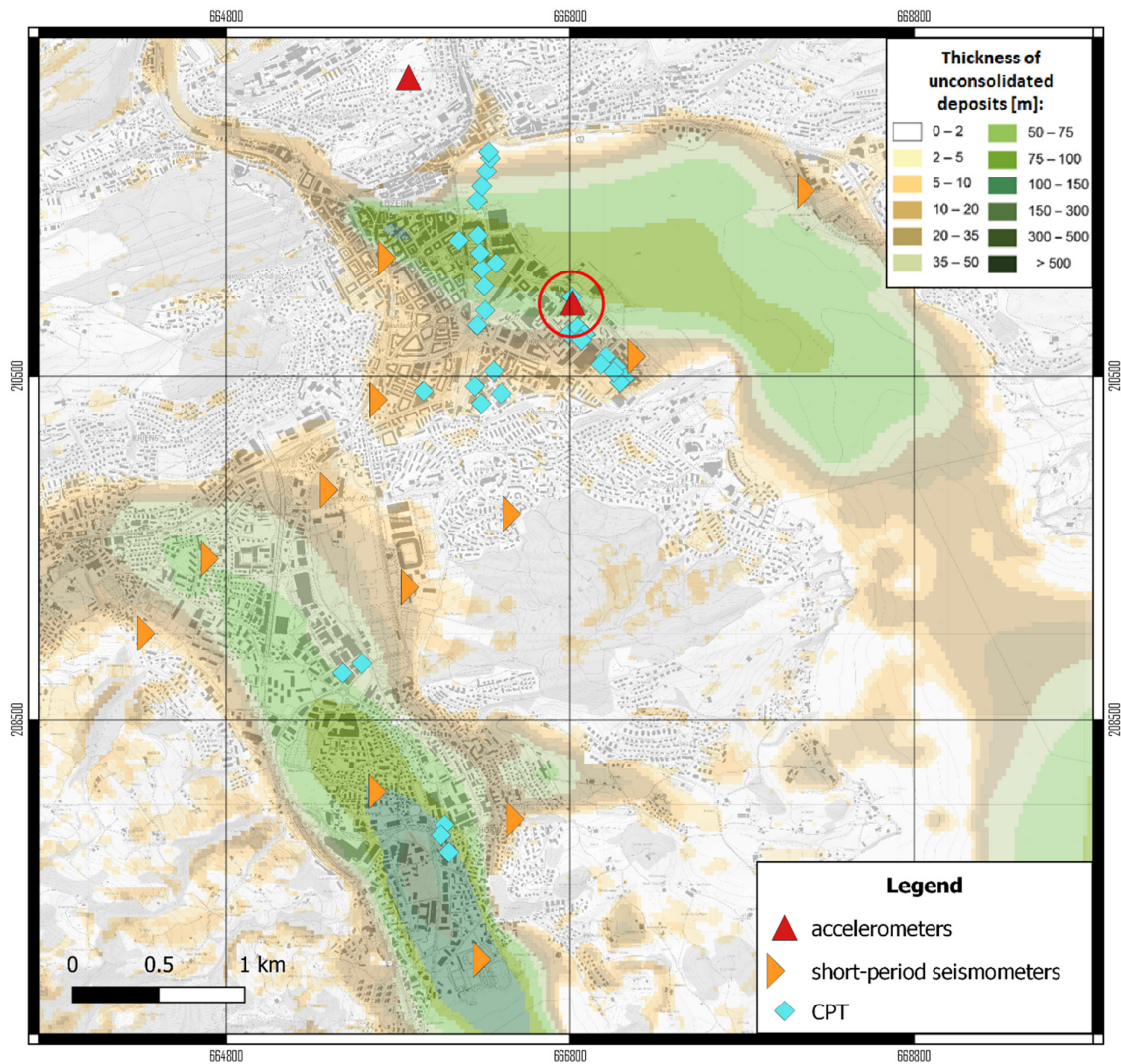
*Figure 2. The thickness of unconsolidated deposits in the Lucerne area according to the Federal Office of Topography (map.geo.admin.ch). The CPT measurements and local seismic monitoring network are shown. Station SLUW is marked using a red circle.*

Even though Central Switzerland is a low-to-moderate seismicity area with very low seismic activity in the last 50 years (Gisler et al., 2004), the seismic hazard cannot be ignored because of several strong historical earthquakes that struck the area. In 1601, the event with a moment magnitude Mw of 5.9 (Fäh et al., 2011) was responsible for serious damage in the city center and for triggering a rock fall from the Bürgenstock and subaquatic landslide followed by a 4–5 m-high tsunami (Schnellmann et al., 2004). Other important events include an earthquake in 1774 (Mw 5.7) and swarms in 1777 (maximum Mw 5.1) and 1964 (maximum Mw 5.3) (Fäh et al., 2011; Gisler et al., 2004). Geological data shows that three even larger paleo-events (Mw 6.5-7.0) probably happened in the area (Kremer et al., 2017; Strasser et al., 2006). The possibility of liquefaction in the Lucerne Lake deposits was mentioned by Siegenthaler et al., (1987), and other authors (Schnellmann et al., 2002) indicating the large deformation of the lake deposits, however, no geological and historical evidence of liquefaction in the city found was published so far. Nevertheless, some indications of

liquefaction structures in cores were found by Keller + Lorenz AG (D. Fäh, personal communication).

The fundamental resonance frequency for the deep parts of the Lucerne basin (>50 m of sediments) is between 1 and 1.5 Hz (Figure 3) as estimated using a dense network of short ambient vibration recordings (Janusz et al., 2021, 2022; Poggi et al., 2012b). The local high-resolution empirical amplification model (Figure 4) that was derived for Lucerne using weak earthquake ground motion and ambient vibration (Janusz et al., 2021, 2022) shows that the amplification factors with respect to the Swiss standard rock profile (Poggi et al., 2011) are more than 10 at the fundamental frequency and remains high (>5) at higher frequencies (up to 5 Hz). In the shallower parts of the basin, the seismic waves will be amplified significantly as well in case of earthquakes. The geophysical investigation at several sites using passive and active seismic measurements shows that sedimentary layers are characterized by very low shear wave velocity (Hobiger et al., 2017; Poggi et al., 2012b, 2013, Figure 6).
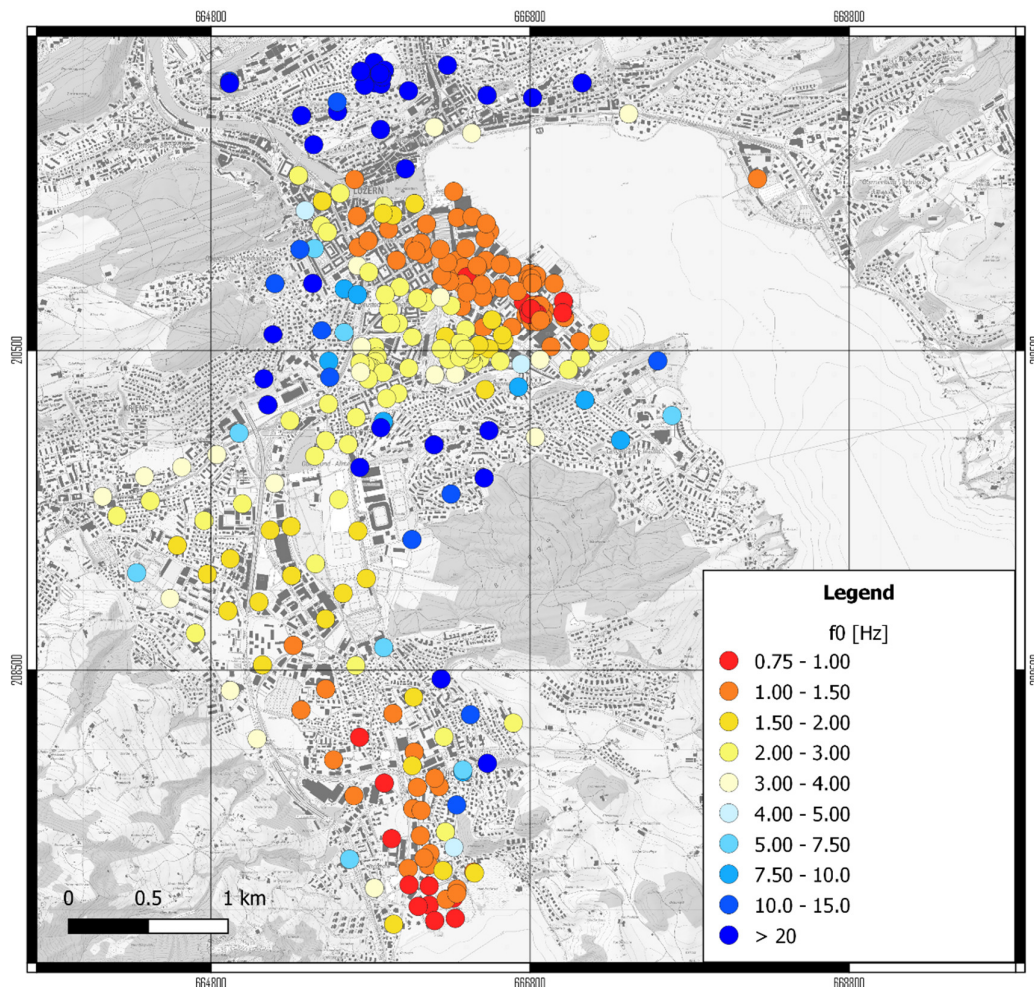


Figure 3. Map of fundamental resonance frequency $f_0$ for Lucerne area derived using H/V ratios using RayDec method (Hobiger et al., 2009).
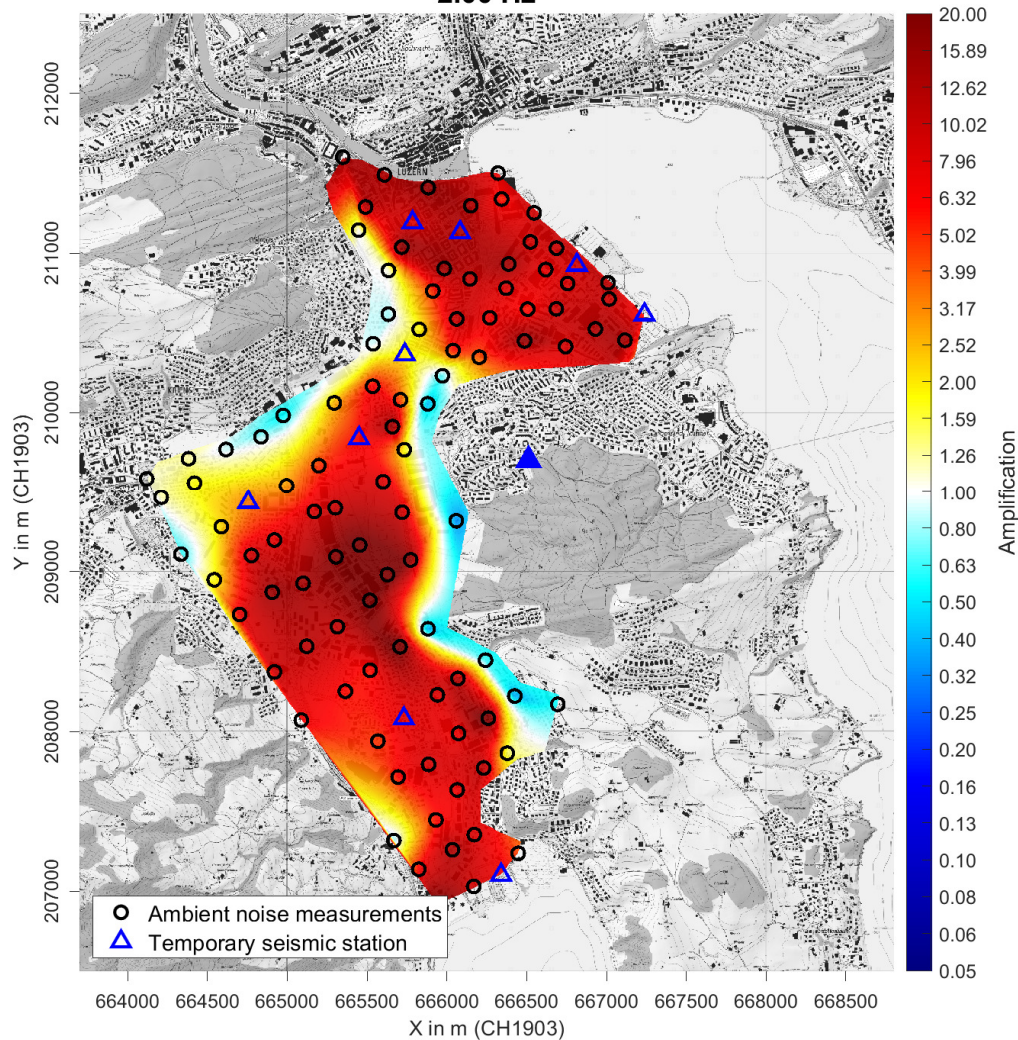
*Figure 4. Amplification factors with respect to Swiss standard rock profile (Poggi et al., 2011) for Lucerne area for 2 Hz using hybrid Standard Spectral Ratio method (Perron et al., 2018). Figure modified from Janusz et al., (2022).*

Several site characterization campaigns were performed in Lucerne during the last 20 years. Thanks to cooperation with the company Geoprofile, we have access to 34 CPT profiles (Figure 2) including two SCPTu measurements. Moreover, geological information and documentation of hundreds of boreholes are available thanks to the help of the administration of Canton Lucerne. We used also passive and active seismic measurements carried out by the Swiss Seismological Service (SED) (Hobiger et al., 2017; Michel et al., 2013; Poggi et al., 2012b; Poggi et al., 2013).

Because of significant lateral variability at a small scale, Lucerne is a very challenging case study in terms of building 2D or 3D models. The work to build a 2D model is still ongoing; hence, we will show the 1D analysis for one chosen site located close to the lakefront in Lucerne city center in the relatively deep part of the basin (70 m of deposits, Figure 2). Federal

8

Office of Topography Swisstopo Swisstopo (https://s.geo.admin.ch/998955831b) classifies the sediments as artificial deposits (Figure 1b). The choice of the site was motivated by the large availability of geophysical data nearby. Since 2010, the permanent accelerometer SLUW belonging to the Swiss Strong Motion Network (SSMNet - Hobiger et al., 2021; Michel et al., 2014) is operating at the site. From now on, the site will be called SLUW in the text. In 2011, as part of the characterization of the seismic station, active and passive seismic geophysical measurements were performed (Poggi et al. 2013) as well as CPT and downhole seismic experiment SCPTu (Geoprofile GmbH, 2013). In addition, a borehole is located 100 m from the site.
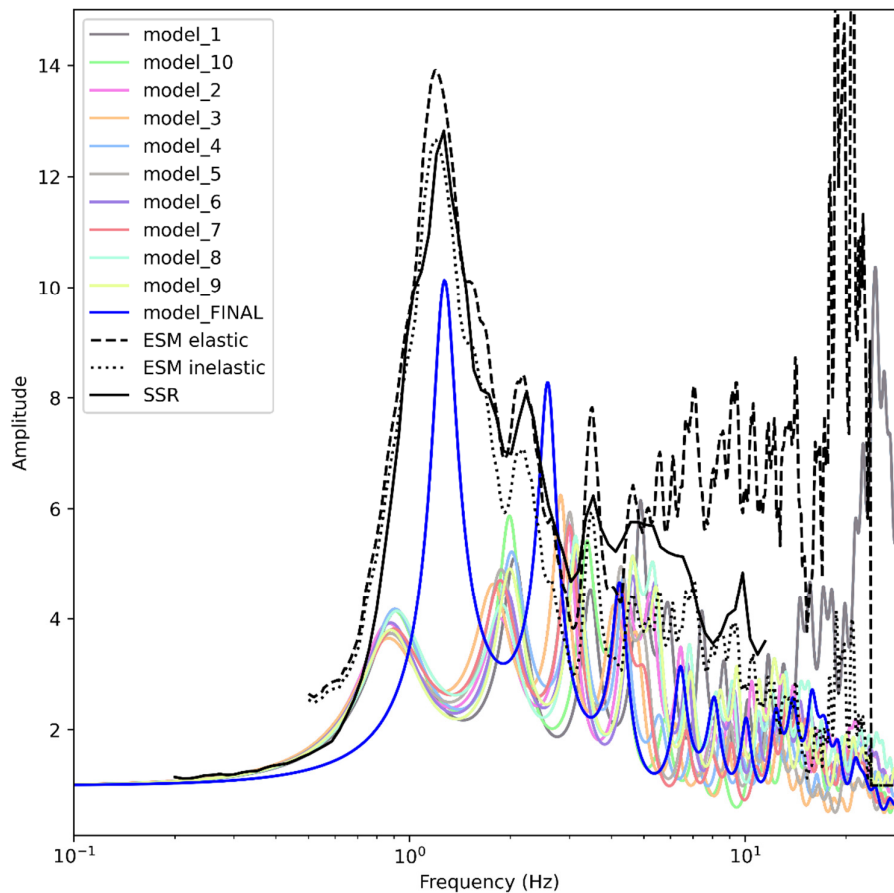


*Figure 5. Site SLUW: 1D linear viscoelastic response simulated for several S-wave profiles compared to empirical amplification function using SSR (Borcherdt, 1970) and ESM (Edwards et al., 2013) methods. All tested velocity models are results of inversion of active and passive seismic. Models from 1 to 10 are without geological constraints and published in Poggi et al., (2013). Model_FINAL is based on the velocity profile that was used for simulations and was inverted using geological constraints (F. Panzera, personal communication). More information is in the text.*

The fundamental frequency at the site is about 1.2 Hz (Poggi et al. 2013). The polarization analysis (Burjánek et al., 2010) shows weak polarization at 1.2 Hz in the direction of the main valley axis (NNW-SSE) which is probably related to 2D/3D resonances (Poggi et al. 2013). The empirical relative amplification function derived using SSR (Borcherdt, 1970) and ESM (Edwards et al., 2013) methods show the peak at 1.2 Hz (Figure 5) with an amplitude of about

12 (Janusz et al., 2021, 2022). The amplification factors decrease gradually from 12 at 1.2 Hz to about 4-5 at 10 Hz showing significantly increased seismic hazard at this site even for high frequencies (Janusz et al., 2021, 2022). The downhole seismic experiment (SCPTu) shows that shear wave velocity is less than 300 m/s for the first 30 m (Geoprofile GmbH, 2013, Figure 6). The shear wave velocity profile up to bedrock was constructed using combined data from active (MASW) and passive (array) seismic experiments (Poggi et al. 2013). The results show a low-velocity layer in the first 10 m followed by a progressive increase of velocity from 300 to 1000 m/s at about 80 m; the bedrock is estimated to be at about 200 m with a velocity of 1800 m/s (Poggi et al. 2013). $V_{s30}$ is 224 m/s which corresponds to soil class D according to the Swiss Building Code classification (SIA261, 2020). The water table is at 0.5 m according to the data from the nearby borehole and the Geoportal Kanton Luzern website (https://geoportal.lu.ch).
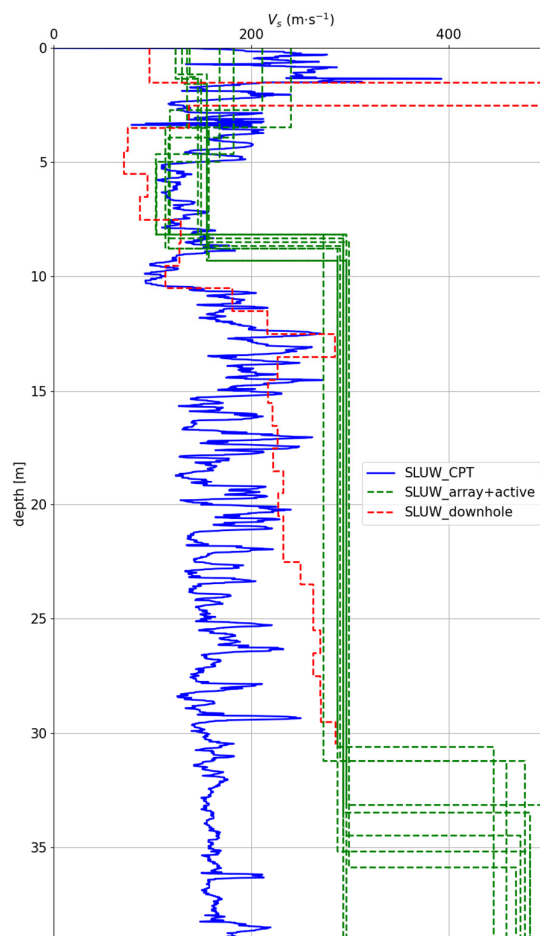


Figure 6. For the site of the strong-motion station SLUW: comparison of shear wave velocity in the first 40 m derived from CPT (blue) using empirical relations (Table 1), an active and passive seismic experiment in green, and a seismic downhole experiment in red.

## 4. Methodology

### 4.1 Building a model

We use all available data (i.e. CPT, seismic data, nearby boreholes, amplification data) to characterize the soil profile, however, for the shallow part of the profile (usually <30 m), the main source is CPT readings. For the deeper part of the basin, geophysical or geological data is used to define the soil properties. Based on CPT, we calculate several geophysical and geotechnical parameters (Table 1) and define several distinctive layers. Then, the mean value of each parameter for each layer is calculated and assigned to the middle of the layer. Because several empirical relations are often described in the literature to estimate one parameter (i.e. shear wave velocity), for some (Table 1), the mean over several realizations is calculated, or one equation is chosen subjectively. It is preferred to use shear wave velocity and density from a downhole seismic experiment or active or passive seismic (if the resolution is high in the shallow part) as an input. However, if such data is not available, the S-wave derived from CPT can be used. In case shear wave velocity and density from seismic are used, they are used also as an input to derive other parameters using empirical relations. Even though the value of the coefficient of Earth pressure at rest $K_0$ is commonly assumed 0.5 (normally consolidated) or 1 (isotropic), we choose to use values calculated using empirical relation (Mayne & Kulhawy, 1983). The influence of some of the parameters was studied (chapter 5.7.7).

Table 2 shows parameters that are needed as input for numerical simulations of wave propagation and inversion for dilatancy parameters. For layers that are prone to liquefaction (i.e. sandy-silty water-saturated layers), 5 dilatancy parameters have to be defined (Table 3). The deeper layers (up to the bedrock) are considered linear and only $V_s$, density $\rho$ and quality factor Q have to be specified.

### 4.2 Inversion for dilatancy parameters

In order to find dilatancy parameters for layers susceptible to liquefaction and cyclic mobility, we follow the procedure of Roten (2014). In the first step, we estimate the cyclic resistance ratio $CRR_{7.5}$ from CPT based on Robertson, (2009) and Robertson & Wride, (1998) which is a cyclic stress ratio required to trigger liquefaction during 15 uniform cycles during the laboratory testing which corresponds to stress excited by magnitude 7.5 earthquake. The lower CSR and equivalently lower the magnitude of the earthquake assuming the same distance, the higher number of uniform cycles are needed to initiate liquefaction. The relation between CSR and the number of uniform cycles (N) is described using the liquefaction resistance curve (LRC) that can be estimated from the $CRR_{7.5}$ value using magnitude scaling factors (MSF) (Idriss & Boulanger, 2006):

$$N = \frac{15}{MSF^{\frac{1}{0.337}}} \tag{1}$$

In this study, we used 14 regularly distributed MSFs values from 1.8 to 0.4 obtaining the LRC curve with 14 distinctive points.

*Table 1. Soil properties needed as an input in performed numerical simulations. If the parameters are calculated from CPT, the empirical relation is given. Several parameters (i.e. the shear wave velocity, density, and friction angle) are calculated as a mean over listed empirical relations. If the shear wave velocity and density can be obtained from geophysical measurements (i.e. passive or active seismic experiment), CPT data is not used.*

| Parameter | Empirical relation / Value / Remarks |
|---|---|
| Tip resistance ($q_c$) [Pa] | Directly from CPT |
| Sleeve friction ($f_s$) [Pa] | Directly from CPT |
| Penetration pore pressure ($u_2$) [Pa] | Directly from CPT |
| Soil behaviour type index ($I_c$) [-] | Robertson & Wride, (1998); Robertson, (2009) |
| Cohesion (c) [Pa] | Mesri & Abdel-Ghaffar, (1993); calculated only if $I_c > 2.5$ |
| Coefficient of the Earth pressure at rest ($K_0$) [-] | Mayne & Kulhawy, (1983) |
| Specific weight ($\gamma$) [N/m$^3$] / density ($\rho$) [kg/m$^3$] | Mayne, (2014); Mayne, (2006); Robertson & Cabal, (2010) |
| $CRR_{7.5}$ [-] | Robertson & Wride, (1998); Robertson, (2009); calculated only if $I_c < 2.7$ |
| Shear wave velocity $V_s$ [m/s] | Hegazy & Mayne, (1995); Hegazy & Mayne, (2006); Mayne, (2007); Robertson, (2012) |
| Friction angle ($\phi$) [°] | Kulhawy & Mayne, (1990); Mayne & Campanella, (2005); Robertson & Campanella, (1983) |
| Phase transformation angle [°] | Ishihara & Towhata, (1982) |
| Porosity [-] | Assumed (0.45) |
| Poisson ratio [-] | Assumed (0.33) |
| Density of water ($\rho_w$) [kg/m$^3$] | 1000 |
| Depth of the water table ($d_w$) [m] | From geological data |
| Hydrostatic pressure ($U_0$) [Pa] | $U_0 = (thickeness - d_w) \cdot 9.81 \cdot \rho_w$ |
| Total vertical stress ($\sigma_v$) [Pa] | $\sigma_v = \rho \cdot 9.81 \cdot thickness$ |
| Vertical effective stress ($\sigma'_v$) [Pa] | $\sigma'_v = (\rho - U_0) \cdot 9.81 \cdot thickness$ |
| Mean effective stress ($\sigma'_0$) | Mean over effective vertical and horizontal stress $\sigma'_0 = \frac{\sigma'_x + \sigma'_v}{2}$, where $\sigma'_x = K_0 \cdot \sigma'_v$ |
| Quality factor (Q) [-] | Assumed (see chapter 4.3) |

*Table 2. Input soil parameters for liquefiable layers for inversion procedure (except Q) and for 1D non-linear simulations (except CRR7.5). The input parameters for the whole profile can be found in Appendix 2.*

| Parameter [unit] | Layer 1 | Layer 2 | Layer 3 |
|---|---|---|---|
| $CRR_{7.5}$ [-] | 0.19 | 0.10 | 0.19 |
| Porosity [-] | 0.45 | 0.45 | 0.45 |
| Shear wave velocity $V_s$ [m/s] | 208 | 128 | 122 |
| Friction angle $\phi$ [°] | 34.6 | 31.5 | 36.1 |
| Phase transformation angle [°] | 23.3 | 21.0 | 24.5 |
| Density $\rho$ [kg/m$^3$] | 1925 | 1778 | 1713 |
| Coefficient of the Earth pressure at rest $K_0$ [-] | 0.74 | 0.69 | 0.76 |
| Mid-depth [m] | 12.15 | 8.45 | 3.3 |
| Thickness [m] | 3.3 | 0.9 | 0.8 |
| Mean effective stress $\sigma'_0$ [kPa] | 80.6 | 50.7 | 26.4 |
| Poisson ratio [-] | 0.33 | 0.33 | 0.33 |
| Q [-] | 30 | 10 | 10 |
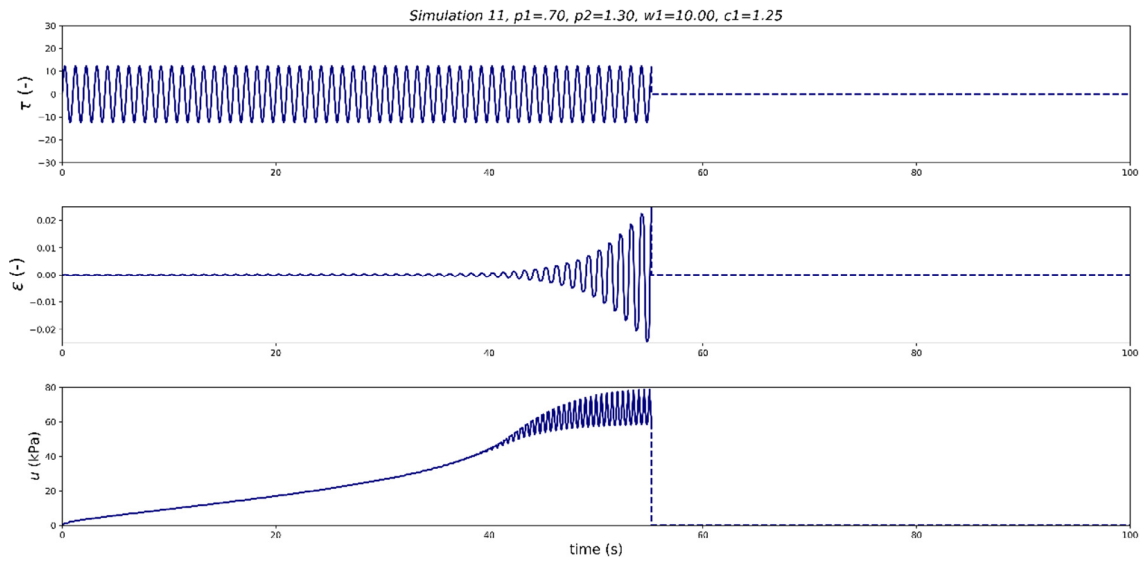


*Figure 7. Example of the simulated stress-controlled experiment for CSR=0.15 and given set of dilatancy parameters. Stress, strain, and pore pressure development are shown. The simulation ends when strain reaches 2.5% which is considered liquefaction onset.*

*Table 3. Set of dilatancy parameters with the lowest misfit for each liquefiable layer together with search ranges.*

| Dilatancy parameter | Search range | Layer 1 | Layer 2 | Layer 3 |
|---|---|---|---|---|
| $p_1$ | 0.4 - 1 | 0.97 | 0.96 | 0.99 |
| $p_2$ | 0.6 - 2 | 1.73 | 1.17 | 1.80 |
| $w_1$ | 0 - 20 | 7.17 | 1.87 | 6.56 |
| $S_1$ | 0.01 | 0.01 | 0.01 | 0.01 |
| $c_1$ | 0 - 2.5 | 0.94 | 0.65 | 0.94 |

The inversion scheme is based on the Neighbourhood algorithm (Sambridge, 1999a, 1999b, 2003). The idea is to divide model space into *n* cells (<u>sample size for the first iteration</u>) and then *x* cells (the <u>number of cells to resample</u>) with the lowest misfit are divided into *y* new cells (*y* is <u>samples of size for all other iterations</u> divided by *x*). Then the process is repeated until a <u>maximum number of iterations</u> is reached. If *x* is low, then only a few best cells are taken and less model space area is explored, if *x* is high, then we explore the model space more widely. If *y* is low, fewer models are tested, so the algorithm is less explorative. Hence, two of the most important parameters controlling the inversion are <u>sample size for all other iterations</u> and the <u>number of cells to resample</u>. The higher these two numbers, the more explorative the algorithm is; the lower, the more exploitative the algorithm, becomes. Last but not least, in order to explore the model space, the <u>maximum number of iterations</u> has to be respectively high to have enough time to search the model space extensively. The values of inversion parameters that are used are shown in Table 4. The parameters were chosen based on the performed tests (chapter 5.7.5).

*Table 4. The parameters to perform an inversion with the Neighbourhood algorithm.*

| Parameter | Value |
|---|---|
| maximum number of iterations | 500 |
| the sample size for the first iteration | 128 |
| samples of size for all other iterations | 128 |
| number of cells to resample | 64 |

We invert for 4 dilatancy parameters ($p_1$, $p_2$, $w_1$, and $c_1$), while $S_1$ is set to a small non-zero value (0.01) for numerical stability. For each CSR value sampled from the LRC curve, the stress-controlled experiment in simple shear mode is simulated using the liquefaction front model by Iai et al., (1990) until the strain reaches 2.5% (5% double amplitude). The code was written by Fabian Bonilla and modified by Daniel Roten. In the used forward model, stress and strain are not scaled, so there is no control of damping. An example of the simulated stress-controlled experiment for CSR=0.15 is shown in Figure 7. Figure 8 shows the stress-strain relation for several CSR (0.34 - 0.095). The applied stress $\sigma_{xy}$ is calculated based on the number of cycles $N$, CSR and mean effective stress $\sigma'_0$.

$$\sigma_{xy} = \sin(2.0 \cdot \pi \cdot dt \cdot (N - 1) \cdot CSR \cdot \sigma'_0 \tag{2}$$

In the process, the new LRC curve is created for a given set of dilatancy parameters and misfit is calculated between data ($n_k$) and model ($x_k$):

$$misfit = \sum_{k=1}^{K} (n_k - x_k)^2 \tag{3}$$

where K is the number of points. The inversion procedure stops after the given number of simulations.
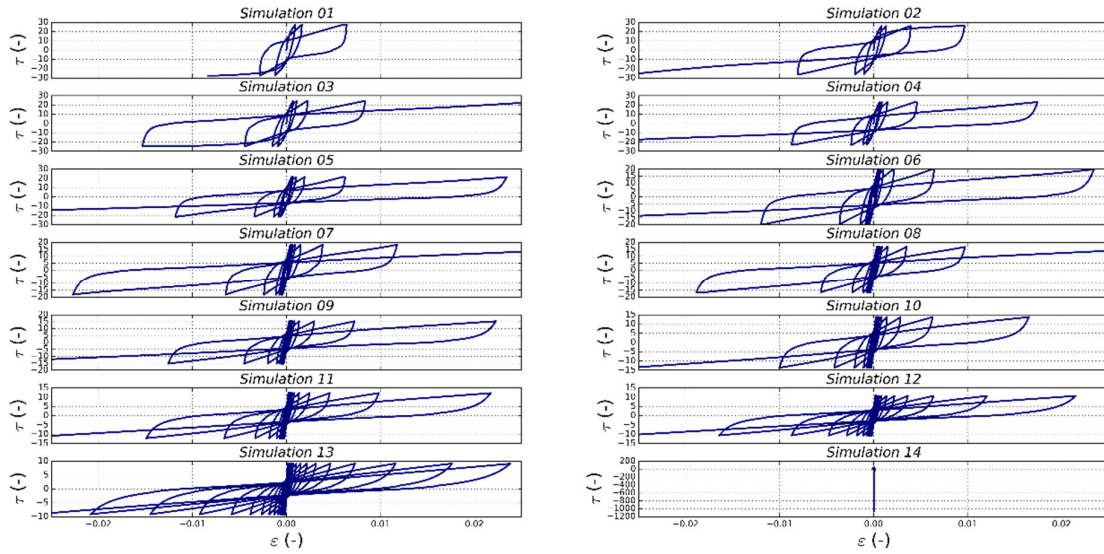
*Figure 8. Stress-strain relations for the stress-controlled experiment for several CSR (between 0.34 to 0.095) where Simulation 01 correspond to the highest CSR. For the lowest value, simulations often fail.*

Figure 9 shows an example of the LRC generated from the $CRR_{7.5}$ value (in black) and the LRC curves tested during one inversion run coloured by misfit where yellow corresponds to the highest and red to the lowest misfit.
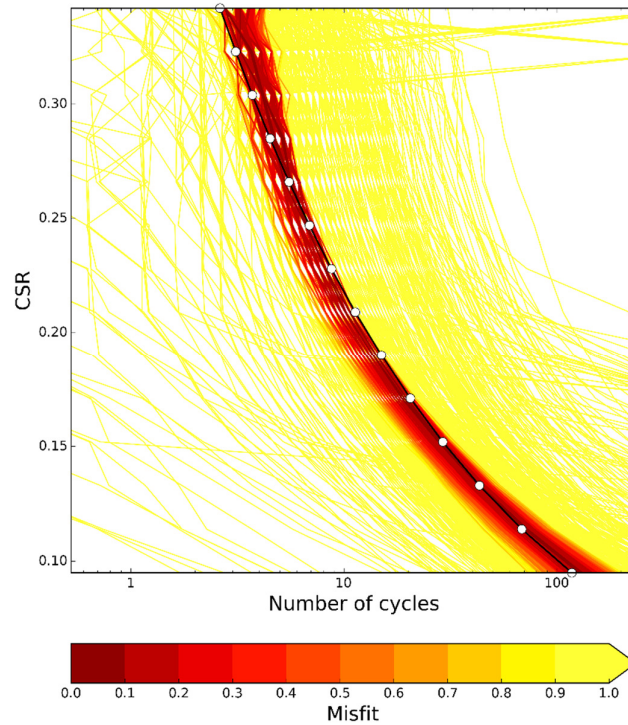


*Figure 9. The input LRC curve (in black) and all LRC curves generated during one run of inversion. Misfit (equation 3) is indicated by colour - the darker red, the lower the misfit of the whole curve. It is an example of the final inversion for layer 1.*

15

### 4.3 1D linear site amplification modelling

For verification of the shear wave velocity profile as well as for assessing the impact of non-linearity for a given input ground motion, we need to calculate the linear transfer function of a soil column. We use code TREMOR written by Fabian Bonilla to compute the viscoelastic linear transfer function in a layered, damped soil on an elastic rock for a given input ground motion. The computation of the viscoelastic linear transfer function implements the constant Q model (Kjartansson, 1979). The needed input soil profile includes shear wave velocity $V_s$, density $\rho$, and quality factor Q, which is inversely proportional to damping. Because we have no information about Q, we tested several approximations:

1)
$$Q \sim \frac{V_S}{10} \text{ (Olsen, 2000)} \tag{4}$$

2)
$$Q \sim \begin{cases} 13 \; for \; V_S < 300 \; m/s \\ -16 + 104.13 \left(\frac{V_S}{1000}\right) - 25.225 \left(\frac{V_S}{1000}\right)^2 + 8.2184 \left(\frac{V_S}{1000}\right)^3 \; for \; V_S > 300 \; m/s \end{cases} \tag{5}$$
$$\text{(Brocher, 2007)}$$

3) Trial and error approach in order to fit empirical amplification function assuming that Q for rock should be >100 and 10-30 for sedimentary layers (F. Bonilla, personal communication)

### 4.4 1D non-linear simulations

For simulating wave propagation in non-linear media, we use a finite-difference code NOAH that is coded using Fortran90. For calculations, we use ETH High-Performance-Cluster EULER, for post-processing and plotting, we used Python.

The code saves the simulated ground motion as well as shear strain and stress, and pore pressure excess at the desired depth, but also at all mesh nodes of the numerical model. In addition, maximum values of acceleration, shear strain, pore pressure excess, etc. for each depth are saved. After running simulations with NOAH, we are able to access the ground motion simulated at each depth using provided post-processing tools.

To account for the uncertainty of inversion for dilatancy parameters, simulations were performed each time for 30 sets of dilatancy parameters with the lowest misfit. In the case of SLUW, cyclic mobility is considered for three layers that are treated separately during the simulations. In addition, the impact of using randomized sets of dilatancy parameters was tested as well as the usage of different precision of the dilatancy parameters.

In order to assess the impact of non-linearity, we compare the non-linear and viscoelastic linear site responses for each input ground motion by calculating the ratio between them. The viscoelastic linear response is calculated using code TREMOR, while non-linear with NOAH. We calculate linear and non-linear spectral ratios with respect to the input ground motion, which is for the rock site:

$$spectal\ ratio = \frac{U_{site}}{U_{rock}} \tag{6}$$

Where U is Fourier amplitude spectra of the ground motion smoothed using Konno & Ohmachi, (1998) algorithm with a b value of 40. Then, the ratio between linear and non-linear responses is calculated.

$$ratio_{\frac{linear}{non-linear}} = \frac{spectral\ ratio_{linear}}{spectral\ ratio_{non-linear}} \tag{7}$$

Moreover, we calculate surface spectral acceleration response spectra from calculated acceleration with 5% of damping for each scenario in order to compare the impact of different input ground motions using a Python package for seismic signal processing (eqsig – doi: 10.5281/zenodo.3263949).

To investigate the possibility of liquefaction, we use the dilatancy parameter S – a value of liquefaction front, which is a ratio of pore pressure excess and effective confining stress. Liquefaction starts when S reaches 0.

As for input ground motion, we use 11 scaled waveforms (Panzera et al., 2021b) made available by an on-going project financed by the Swiss Federal Office for the Environment (FOEN). The waveforms were selected using Baker & Lee, (2018) algorithm considering a new Eurocode 8 criteria (EC8, draft) and scaled to represent the elastic response spectrum in the period range 0.02-2 s for soil class A and building importance class III of the Swiss building code SIA 261 (SIA261, 2020) corresponding to about 975 year return period. While the lower limit (0.02 s) was the maximum sample frequency of some old waveforms, the upper limit (2 s) is related to the minimum resonance frequency observed in Switzerland excluding deep alluvial basins, and to the low-frequency content of available accelerograms. It was ensured that at each period, the ratio between the mean over the 5%-damped response spectra of the set and the target spectrum is neither larger than 1.3 nor smaller than 0.75. At the same time, the mean of such ratios over the whole considered period range is not lower than 0.95 and each accelerogram of the set is above 50% of the target spectrum. Because soil class A waveforms at short distances (≤ 20 km) and magnitudes (≥ 5.0) were only a few, the database was extended to the sites with $V_{S30}$ ≥ 700 m/s since generally no resonance is observed for such sites (Poggi et al., 2012a). The waveforms were selected from the following strong-motion databases: the Engineering Strong Motion database (https://esm-db.eu/#/home) and the Japanese database of K-NET and KiK-net (https://www.kyoshin.bosai.go.jp). In the chosen set, there are not two waveforms of the same three-component record or more than two records of the same earthquake.

Since the Lucerne area is located at the border of those seismic zones (https://s.geo.admin.ch/99b32e74cf), we used 2 sets of 11 waveforms respectively for seismic zones Z1B and Z2 (SIA261, 2020). By using building importance class III, the resulting seismic hazard is for a return period of about 975 years, however, for some experiments, we used also another set of waveforms that correspond to about a 475-year return period

(building importance class I). If not specified, the presented results are for a return period of about 975 years. Because it is surface motion, we divided the time series by 2 to take into account the free surface effect, and we use elastic boundary conditions.

## 5. Results and discussion

### 5.1 CPT interpretation and comparison

Figure 1 in Appendix 1 shows the final model for site SLUW for the first 30 m. It consists of 7 layers, three of which are considered predominately sandy and saturated, hence prone to liquefaction. The soil type and soil parameters are estimated from CPT data using empirical relations (Table 1), while shear wave velocity and unit weight are taken from the downhole seismic experiment (Poggi et al., 2013). We modified $V_s$ and $\gamma$ profiles by removing two layers with unreasonable values (Figure 6) at around 2 and 13 m. The shear wave velocity is very low, below 10.5 m is on average about 100 m/s, and then increases gradually from 200 to 250 m/s from 10.5 to 30 m.

In the shallow part of the soil column, we observe intermixed layers of sand, silts, clays, and organic soils, while below about 14 m, the dominating lithology are clays and organic soils (Figure 1 in Appendix 1). The water table is at 0.5 m. We compare the profile with a nearby borehole (100 m distance) observing the consistency of main lithology and depths of interfaces showing that interpretation based on CPT provides a reasonable approximation of the site. However, the derived soil geotechnical and geophysical parameters cannot be verified using available data. The uncertainty involved in deriving soil properties from CPT using empirical relations is generally high, especially for estimating shear wave velocity; hence, it should be accounted for in further calculations. In addition, the pore pressure sensors were unavailable for SLUW preventing the application of corrections of $q_c$ to obtain corrected total cone resistance $q_t$ (Robertson, 2009).

We compare the shear wave velocity from CPT to $V_s$ profiles from seismic experiments (Figure 6). Profiles from active seismic (MASW) and passive array have a relatively low resolution at shallow depth, while for the first 8 m, the values are similar. However, the resolution of seismic data for such depths is not very reliable; below 8 m, S-wave velocity from CPT is underestimated compared to passive. On the other hand, the shear wave velocity from the downhole seismic experiment matches the CPT estimation up to about 15 m. Below that, the SCPTu profile shows a gradual increase of velocity with depth, while $V_s$ from CPT, remains stable with depth (about 170 m/s). The presented comparison shows that CPT can provide only approximated values of $V_s$, but results from passive and active seismic have often too low resolution at shallow depth. Hence, if downhole seismic is not available, CPT estimation of the S-wave velocity can provide a more detailed and reasonable shear wave velocity profile at shallow depth. When it comes to density, the estimates from CPT are generally lower when compared to downhole seismic.

### 5.2 Inversion for dilatancy parameters

Three layers are chosen as potentially liquefiable and we try to find dilatancy parameters for them. We perform several tests presented in chapter 5.7 to find optimal inversion

parameters. Finally, the inversion was performed for a given soil (Table 2) and inversion parameters (Table 4). The results with the lowest misfit for each layer as well as model searching ranges are listed in Table 3.

Figure 10, Figure 11, and Figure 12 show the sets of dilatancy parameters (blue dots) tested during the final inversion run for each of the layers with the best set marked using a vertical black line (Table 3). The red dots indicate the 30 unique sets with the lowest misfit considering two meaningful digits. For layers 1 (the deepest, Figure 10) and 3 (the shallowest, Figure 12), the results for $c_1$ and $w_1$ approach one value, which is similar for both layers, while $p_1$ and $p_2$ show more dispersion with more than one minima, however, values keep approaching the maximum of the search range that is also shown in other experiments. In the case of layer 2 (Figure 11), $c_1$ and $w_1$ converge to one value, however, much lower than in the case of layers 1 and 3. $p_2$ is more variable with two main minima visible. On the other hand, initial dilatancy $p_1$ cannot be unambiguously resolved, even though we can distinguish one main minimum; we observe a cloud of points with similar misfits in the wide area of the model space. It is even more pronounced in some of the experiments that we performed in which the results for $p_1$ were distributed evenly over the whole model space. It shows that the inverse problem is highly non-linear and non-unique. Several sets of dilatancy parameters can sometimes explain the data similarly which should be taken into account while assessing uncertainty.
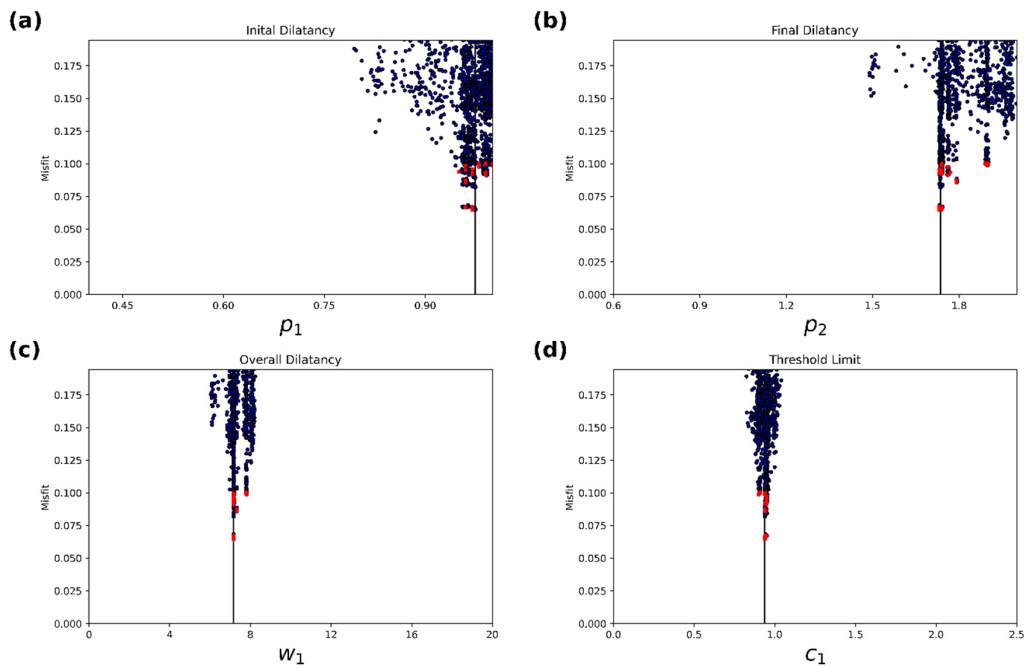


*Figure 10. Sampled sets of dilatancy parameters (in dark blue) during one inversion run for layer 1. The value with the lowest misfit is marked using a black line while the 30 best models are shown using red circles.*
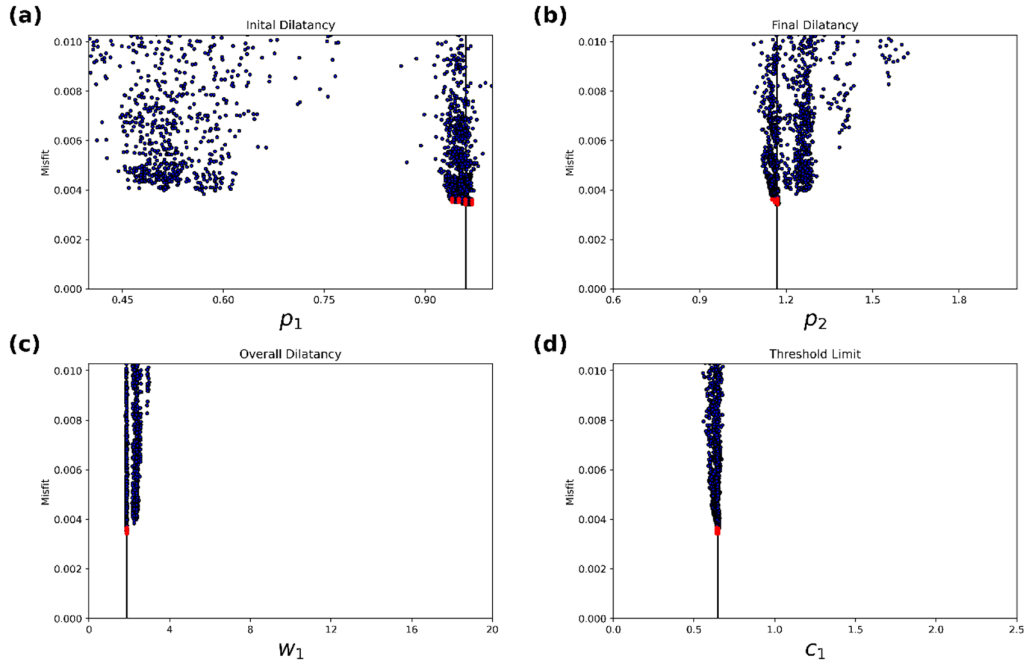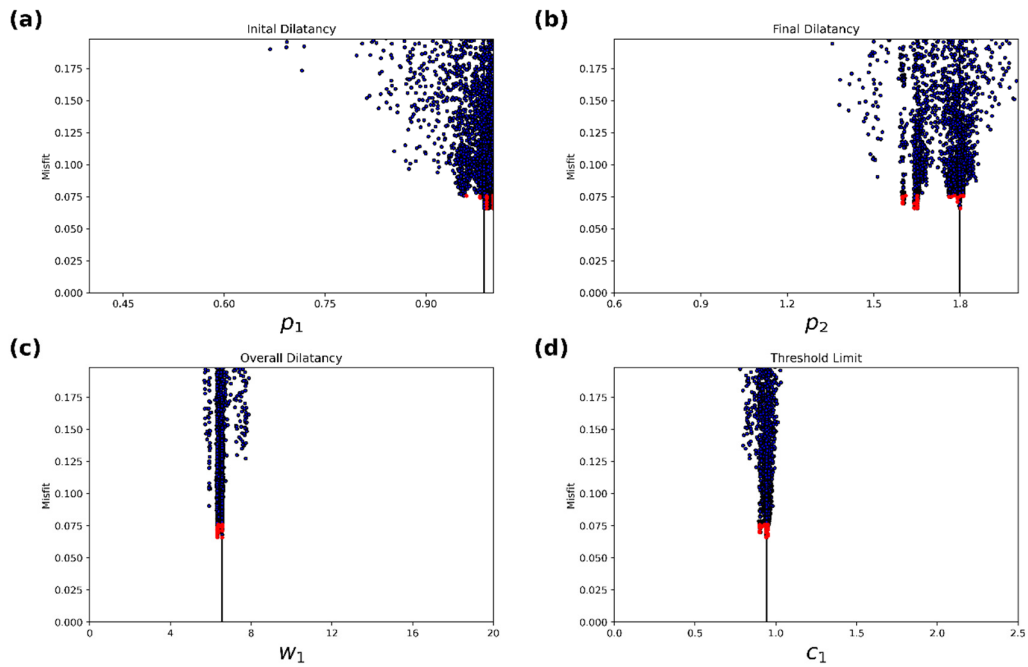
*Figure 11. Sampled sets of dilatancy parameters (in dark blue) during one inversion run for layer 2. The value with the lowest misfit is marked using a black line while the 30 best models are shown using red circles.*



*Figure 12. Sampled sets of dilatancy parameters (in dark blue) during one inversion run for layer 3. The value with the lowest misfit is marked using a black line while the 30 best models are shown using red circles.*

### 5.3 Final model and 1D linear modelling

The final model is defined in the first 30 m using CPT and downhole seismic experiment, while below up to the bedrock; it is calibrated using a shear wave velocity profile from active and passive seismic data. Shallower layers are considered non-linear with three layers prone to cyclic mobility, while the deeper part of the profile is assumed linear (Appendix 2).

However, the linear viscoelastic transfer function of a profile modelled using TREMOR shows great discrepancies between empirical amplification functions estimated for this site using SSR (Borcherdt, 1970) and ESM (Edwards et al., 2013) approaches (Figure 5). Obviously, modelled and empirical transfer functions can be significantly different due to many reasons such as 2D/3D effects, non-linearity, or wrong S-wave or attenuation model. The site is expected to be affected by 2D/3D effects because of the complex basin shape, which is partially confirmed by the results of polarization analysis (Poggi et al., 2013), however, the difference, especially, the shift of fundamental resonance frequency, cannot be simply explained only by 2D/3D site effects. Hence, we tested other velocity profiles in order to find one that better reproduces the empirical amplification function. The best of investigated models is a profile (Figure 13) inverted by F. Panzera from passive and active seismic using geological constraints. This model is used for further simulations. It is characterized by a strong velocity contrast between sediments and bedrock with an interface at about 65 m. According to the map of the thickness of unconsolidated sediments issued by the Federal Office of Topography (https://s.geo.admin.ch/998955831b), the bedrock is at about 70 m, while the previous velocity profile (Poggi et al., 2013) placed it at about 200 m with much weaker velocity contrast. In the study by Poggi et al., (2012a) where the ellipticity of the Rayleigh wave from single station measurements together with generic shear wave velocity profile for the basin are used to better constrain the bedrock depth, the estimated thickness of the sediments at SLUW site is about 130 m. However, the following bedrock depth model (Poggi et al.,2012a) needs to be updated using new single station data and shear wave velocity profiles.

In order to find the attenuation values, we tested several approaches, mainly the assumption that Q is equal to $V_s$ divided by a factor of 10 (Olsen, 2000), the equation of Brocher, (2007) as well as using a simple trial and error method. After comparing the modelled viscoelastic transfer function to the empirical one, we concluded that the best model is:

$$Q = \begin{cases} 10 \; for \; V_S < 150 \, \dfrac{m}{s} \\ 30 \; for \; V_S \in (150, 300) \, \dfrac{m}{s} \\ 40 \; for \; V_S \in (300, 400) \, \dfrac{m}{s} \\ 45 \; for \; V_S > 400 \; \dfrac{m}{s} \\ 100 \; for \; rock \end{cases} \qquad (8)$$

The final shear wave velocity model, extending to bedrock, estimated to be at about 65 m is plotted in Figure 13. The parameters for 3 liquefiable layers are shown in Table 2 and Table 3. Other parameters of the soil column are shown in Appendix 2.
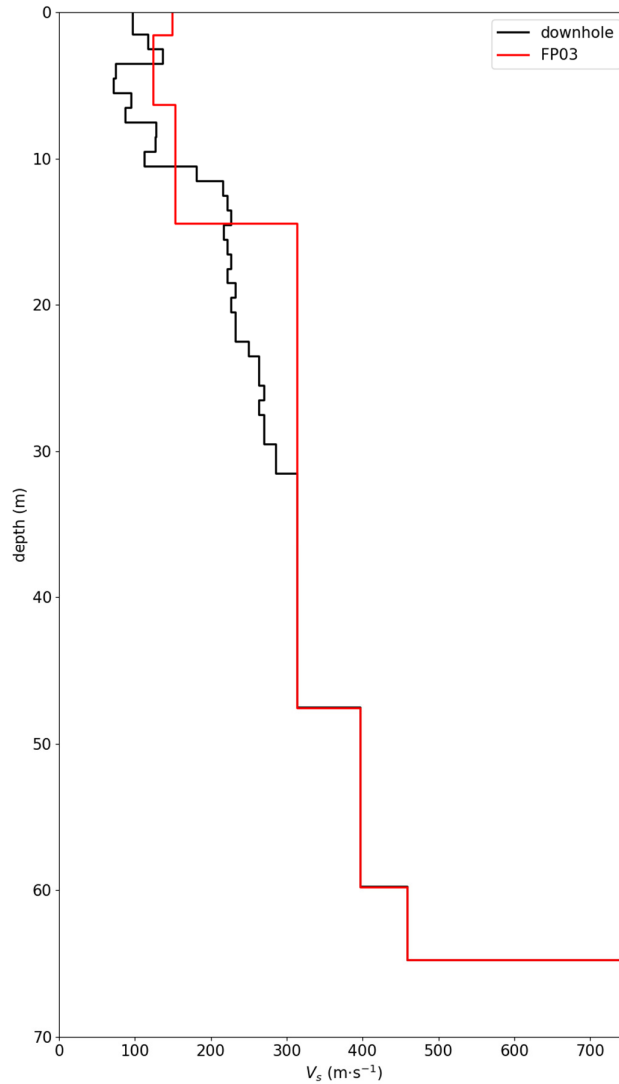


*Figure 13. Final shear wave velocity profile for SLUW used for wave propagation simulations. In the upper part (above 31.5 m), smoothed $V_s$ profile from downhole seismic (black) is used, below – S-wave profile from active and passive seismic (red) inverted with geological constraints (personal communication, F. Panzera). The bedrock is at 65 m with a shear wave velocity of 2333 m/s.*

## 5.4  1D non-linear modelling

In Figure 14, the simulated wave propagation at the surface for SLUW for one random ground motion for seismic zone Z1b (SIA261, 2020) is shown. There is no variation of pore pressure because the first 0.5 m is not saturated. For a given example, we see displacements reaching 10 cm and acceleration of about 1 m/s². Strain-stress relation is approximately linear but some hysteretic behaviour can be observed. On the acceleration plot, we see the ground motion at the rock site (in red) that was divided by 2 to account for free surface effects and

22

applied as input at bedrock depth. The resulting acceleration-time history is lacking high-frequency content compared to the input. While for the P-wave part, the output has higher amplitude, for S-wave, there is no amplification and the de-amplification is observed for surface waves. Figure 15 and Figure 16 show examples of the results in fully saturated sandy layers. At the depth of 8.5 m (layer 2), we observe strong hysteretic behaviour of stress-strain relation. Pore pressure excess is about 50 kPa and normalized pore pressure excess expressed using dilatancy parameter S reaches 0 which means that pore pressure excess is equal to initial confining pressure, which is a sign of liquefaction. We observe also the onset of the liquefaction on the stress-confining pressure plot. For 12 m (layer 1), we observe pore pressure build-up, however, we do not see liquefaction, and the value of S is relatively high. In addition, the stress-strain relation shows more linear behaviour than in the previous example.
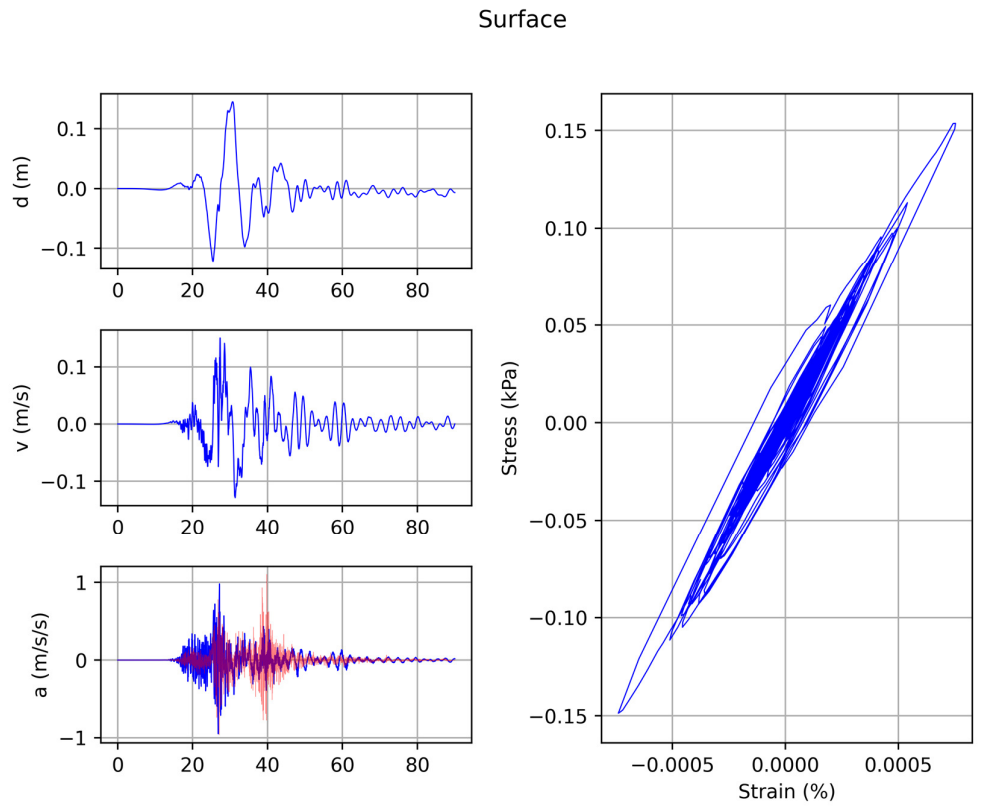
Surface



*Figure 14. An example of the results of 1D non-linear simulation at the surface for one of the ground motions for seismic zone Z1b (SIA261, 2020). In the left panel from the top is shown displacement (d), velocity (v) and acceleration (a). The resulting acceleration history (in blue) is compared to the ground motion at the rock site (in red). On the right, the stress-strain relation is plotted.*

For SLUW, we simulated wave propagation considering non-linear media using several input ground motions and using different 30 sets of dilatancy parameters for each one. We present the results when we investigate the impact separately for layer 1 and layer 2. We do not test the influence for layer 3 because it is very thin (only 0.8 m) as well as it has similar properties to layer 1. To illustrate the impact of changing sets of dilatancy parameters for each ground motion, we plot response spectra at the surface, change of PGA with depth as well as a ratio

of linear and non-linear responses. Because the thickness of the sandy saturated layers in this profile is relatively small, the influence is not significant. In addition, in most of the cases, the spread of chosen 30 sets is not large (Figure 10 and Figure 11). The variability of surface response spectra (Figure 17), PGA (Figure 18), and spectral ratios (Figure 19) for layer 2 for one of the input ground motions are shown, however, the differences are not significant and can be ignored. For layer 1, we see almost no difference. The reasons may be that the sets of dilatancy parameters are more different for layer number 2 (i. e. $p_1$ had several minima); however, layer 2 is thinner than layer 1. Generally, sandy saturated layers may be too thin for the case study site to produce enough changes in the pore pressure to observe the impact of dilatancy parameters. Nevertheless, we will test another site where the shallow part of the soil profile (about 25 m) consists mainly of sandy saturated layers; hence we expect a more pronounced influence. Moreover, we plan to test the influence of other parameters for this and other sites (i.e. $V_s$, density, etc.). We intend also to investigate more the impact of non-linearity with depth to assess which layers are the most affected.
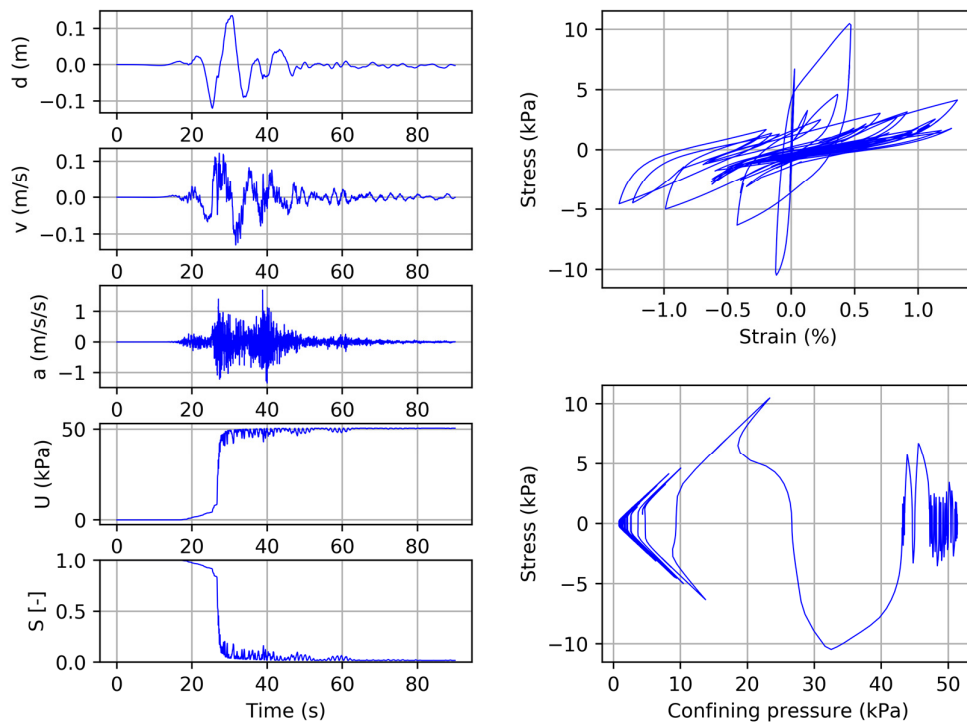
Depth = 8.5 m



*Figure 15. An example of the results of 1D non-linear simulation at depth of 8.5 m (layer 2) for one of the ground motions for seismic zone Z1b (SIA261, 2020). In the left panel from the top is shown displacement (d), velocity (v), acceleration (a), pore pressure (U), and dimensionless dilatancy parameter S indicating liquefaction onset (S=0). In the right panel from the top: stress-strain relation and stress-confining pressure relation.*

However, what can be observed in the following examples (Figure 17 and Figure 19) is the high impact on non-linearity for chosen input ground motion. The resulting response spectrum (Figure 17) is significantly lower compared to results from linear simulations as well

as lower than the elastic response spectrum for soil class D (SIA261, 2020) showing significant de-amplification at a broad range of periods, while in the linear case, we observe substantial amplification for periods lower than 1 s. In addition, the resulting response spectrum is of similar amplitude to the response spectrum of input ground motion. Moreover, in Figure 19 showing linear and non-linear spectral ratios, we observe that above about 1 Hz, the output ground motion is almost completely damped due to the non-linear site effects with visible de-amplification at even higher frequencies.
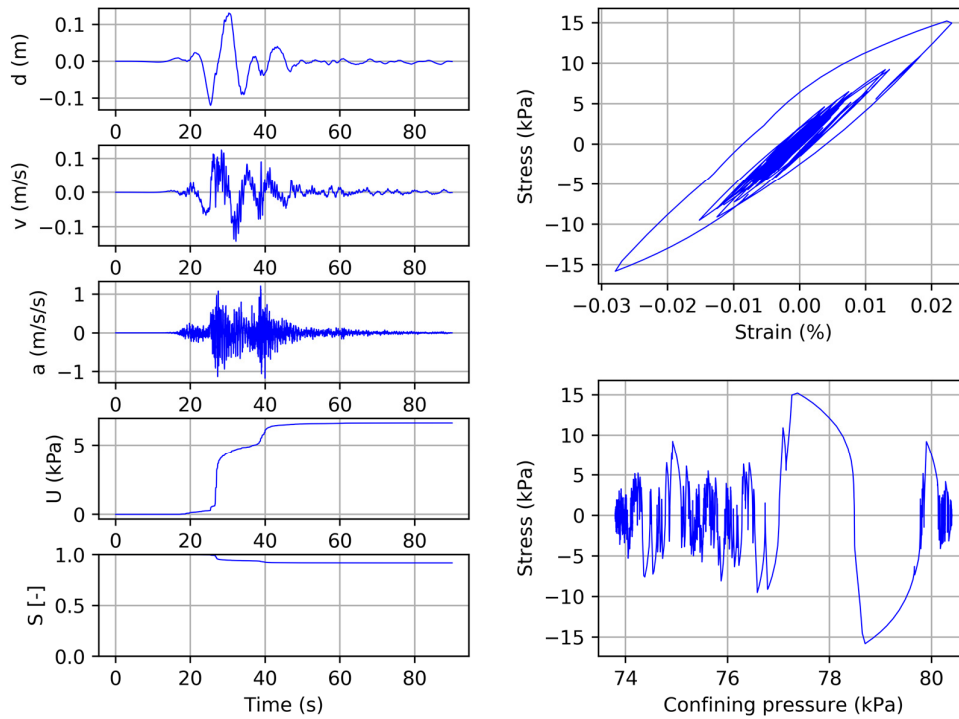


Figure 16. An example of the results of 1D non-linear simulation at depth of 12 m (layer 1) for one of the ground motions for seismic zone Z1b (SIA261, 2020). In the left panel from the top is shown displacement (d), velocity (v), acceleration (a), pore pressure (U), and dimensionless dilatancy parameter S indicating liquefaction onset (S=0). In the right panel from the top: stress-strain relation and stress-confining pressure relation.

While we do not see the impact of dilatancy parameters for chosen example, we observe significant variability in the results depending on the input ground motion. Hence, it is crucial to consider many input ground motions while simulating non-linear soil response. In Figure 20, each of the plotted response spectra at the surface represented by different colors corresponds to one of 11 ground motions from seismic zone Z2 (SIA261, 2020). Because we tested simultaneously the influence of the set of dilatancy parameters, the thickness of each line represents that variability. For response spectra (Figure 20), the variability depending on the different ground motions is quite pronounced, however, all curves are much lower than normative elastic response spectra for soil class D (SIA261, 2020), especially below 1 s. Values exceed 3 m/s$^2$ for some of the ground motions and reach 2 m/s$^2$ for almost all. However,

when we compare linear response spectra (Figure 21) calculated using acceleration modelled using TREMOR, the values are much higher for low periods (>7 m/s$^2$, exceeding 15 m/s$^2$) while similar for longer periods (> 1s). The reason is probably the huge amplification factors for the site (more than 10 times), while considering the non-linear site effects, not only the significant linear amplification is canceled but we observe the reduction of the ground motion compared to the input. It shows that in the case of Lucerne, analysing only linear site response for strong input ground motion gives conservative results, especially at short periods (> 1s). It is worth mentioning that the uncertainty (Figure 21) shown as a standard deviation, is higher for linear response, indicating higher variability of the linear response compared to non-linear considering 11 tested input ground motions.
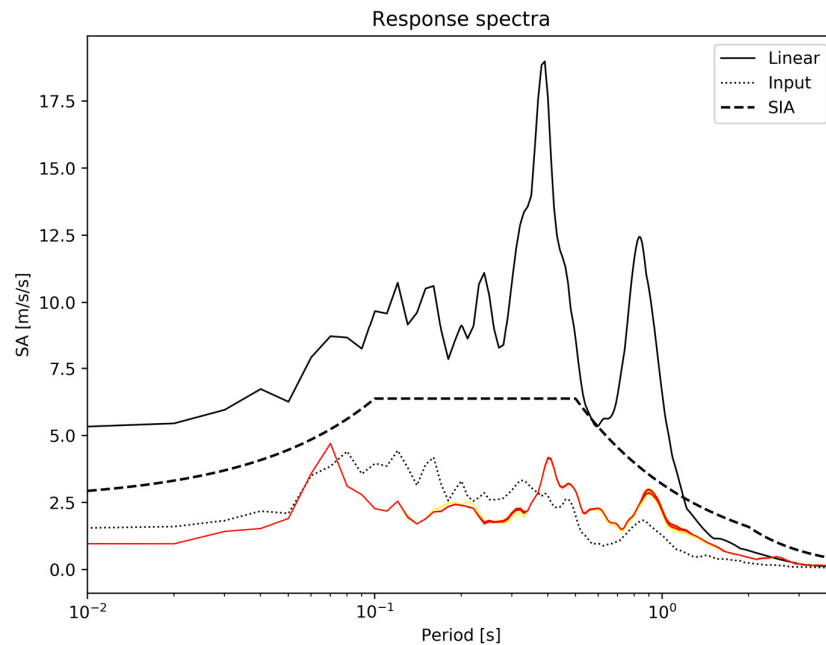


*Figure 17. The variability of resulting response spectra depending on the chosen set of dilatancy parameters for layer 2 for one of the ground motions for seismic zone Z2 (SIA261, 2020), where red is the set with the lowest and yellow with the highest misfit out of the set. The black dashed line shows the elastic response spectrum for soil class D and building importance class III in seismic zone Z2 (SIA261, 2020). The dotted black line is a response spectrum for the rock site and the black solid line is the resulting response spectra if the linear viscoelastic response is simulated.*

We compare the difference between linear and non-linear spectral ratios for each scenario observing a similar pattern. In Figure 22, for an example of 11 ground motions for zone Z2 (SIA261, 2020), the non-linear response is often 2-3 times higher (even up to 10 times) than linear for frequencies lower than about 0.8 Hz, while for higher frequencies (>0.8 Hz), the amplitude of linear transfer function is about 2-5 times higher (exceeding 10 as well). The ground motion amplification in the non-linear case is completely reduced or even de-amplification is visible. Our observations agree with the fact that damping when considering non-linear behaviour is more pronounced at higher frequencies reducing the amplification compared to the linear case. In addition, the variability for different ground motions is significant, especially at low frequencies while the variability due to the change of dilatancy parameters (showed as a thickness of the line) is almost invisible. The results show that

considering non-linear site response in the case of Lucerne is important at low frequencies below 1 Hz.
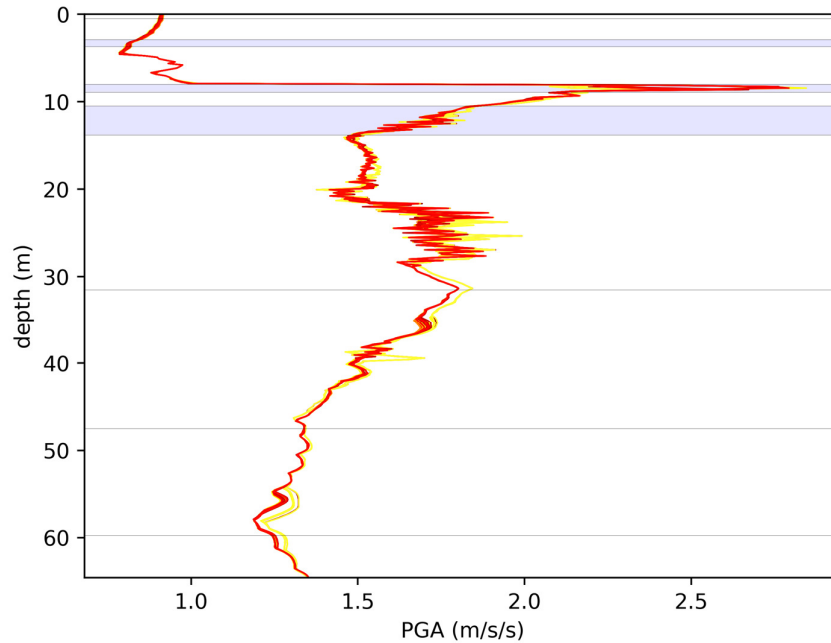


*Figure 18. The variability of the resulting PGA with depth depending on the chosen set of dilatancy parameters for layer 2 for one of the ground motions for seismic zone Z2 (SIA261, 2020), where red is the set with the lowest and yellow with the highest misfit out of the set. Grey lines represent layers' borders while blue rectangular are liquefiable layers.*
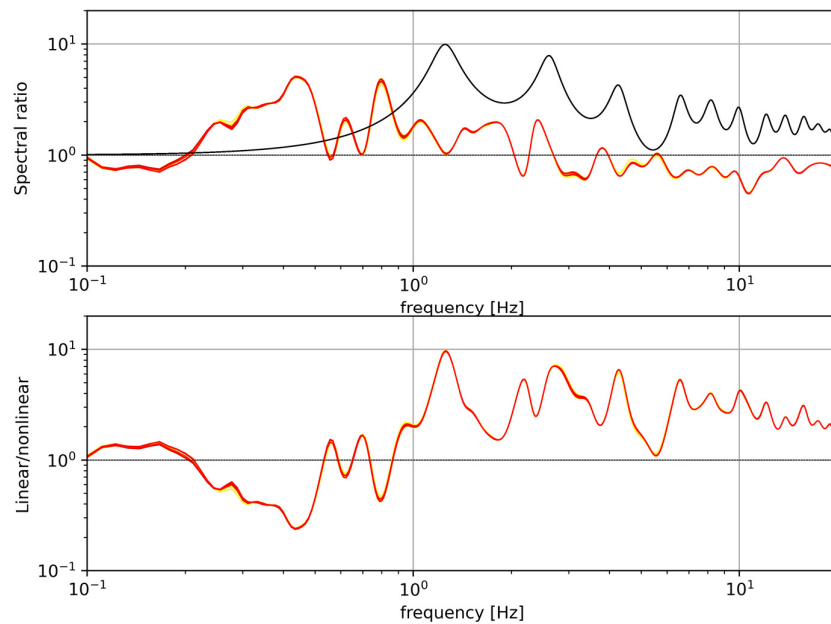


*Figure 19. The variability of the resulting non-linear spectral ratio (top plot) and linear/non-linear ratio (bottom plot) depending on the chosen set of dilatancy parameters for layer 2 for one of the ground motions for seismic zone Z2 (SIA261, 2020), where red is the set with the lowest and yellow with the highest misfit out of the set. The black line in the top plot represents the linear response.*
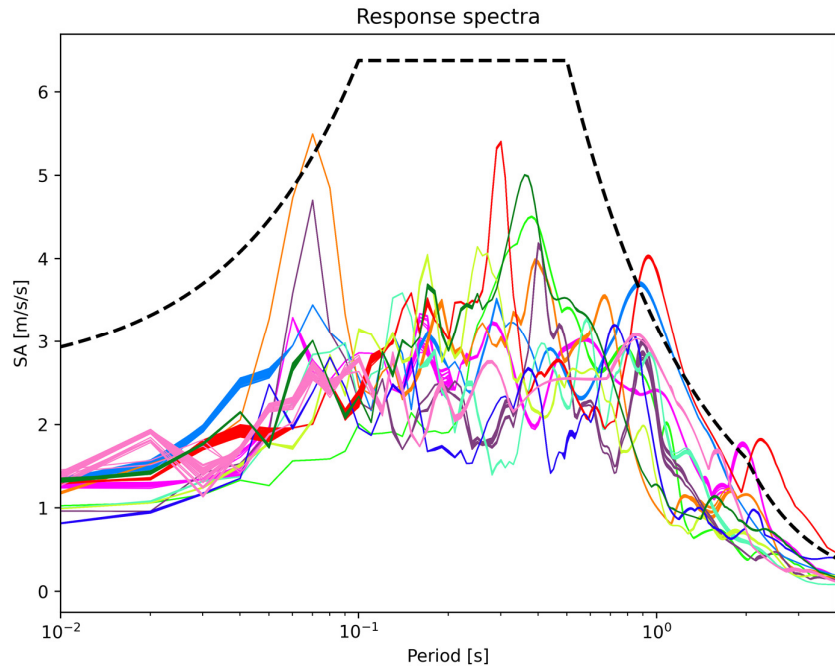
*Figure 20. The response spectra for all ground motions for seismic zone Z2 (SIA261, 2020), one colour represents one input ground motion. The simulations were performed while changing dilatancy parameters for layer 2 and the resulting variability is represented here by the line thickness. The black dashed line shows the elastic response spectrum for soil class D and building importance class III in seismic zone Z2 (SIA261, 2020).*
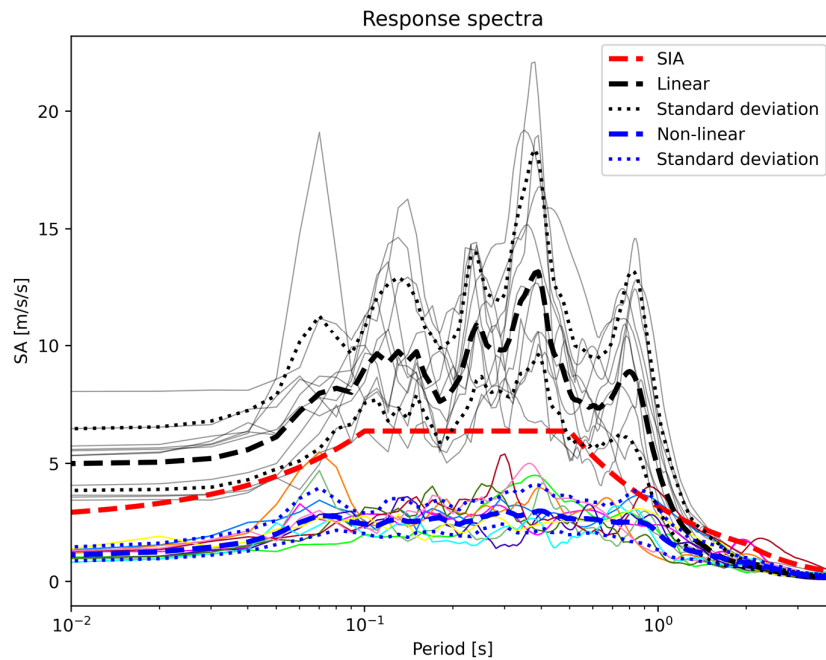


*Figure 21. The non-linear response spectra for all ground motions in seismic zone Z2 (SIA261, 2020), each colour represents one input ground motion, while the grey solid lines are response spectra calculated if the linear viscoelastic response is simulated. The red dashed line shows the elastic response spectrum for soil class D (SIA261, 2020). The black and blue dashed lines show the geometric mean of all showed linear and non-linear response spectra, while dotted lines – standard deviation.*
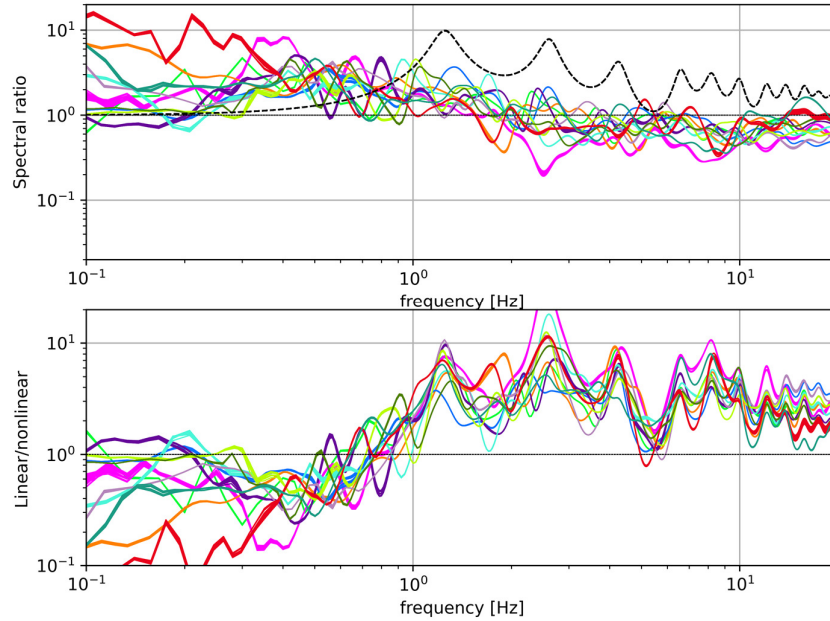
*Figure 22. The spectral ratios for all ground motions in seismic zone Z2 (SIA261, 2020), one colour represents one input ground motion. The simulations were performed while changing dilatancy parameters for layer 2 and the resulting variability is represented here by the line thickness. The black dashed line in the top plot is the linear response.*

Figure 23 shows a variation of PGA with depth for the different ground motions for zone Z2 (SIA261, 2020). Generally, PGA for zone Z2 is higher than Z1b. Moreover, we observe higher PGA when considering the variability of dilatancy parameters for layer 2. The layers' borders are shown using grey horizontal lines while liquefiable layers are marked with light blue rectangular. We observe a peak at about 8-9 m reaching 12-14 m/s$^2$ for some input ground motions. For the rest of the profile, the values are approximately between 1-3 m/s$^2$ depending on the layer and input ground motion.

In all presented examples so far, we see a high impact of non-linearity, however, the sandy saturated layers for the SLUW site are very thin, so at another site with thicker liquefaction-prone layers, the changes in the pore pressure may be even higher, and generate even more significant non-linear behaviour. Another issue is the frequency content of the input motion, which may be not completely coincident with the resonance frequency of the soil in the model reducing the observed effect.

### 5.5  More on the influence of ground motion selection

As discussed, we observe strong variability in the results due to the input ground motion. We cannot hence in practice predict exactly the non-linear response based on previous events. However, we want to answer the question of the minimum amplitude of the ground motion from which we start to observe strong non-linearity which is an important issue while assessing the seismic hazard. When comparing the mean non-linear response calculated over 11 scaled input ground motions for seismic zones Z1b and Z2 (SIA261, 2020) for a return period of 975 years, the difference is negligible (Figure 24). In another experiment (Figure 25), we compare the average results for respectively 11 waveforms for return periods of about

975 and 475 years as well as 475 years divided by 1.6 which approximates the input ground motions representing the uniform hazard spectrum. We observe that the effect of non-linearity is reduced with decreasing amplitude of the ground motion, however, even for the weakest example (i.e. waveforms for a return period of about 475 divided by 1.6); the non-linear soil response is not negligible. Finally, we compare the spectral ratio for the same ground motion but when its amplitude is reduced respectively by the factor of 2, 3… and 100 (Figure 26). The impact of non-linearity decreases fast with reduced amplitude of the ground motion. While for the input ground motion divided by 2, we still clearly see the difference with linear spectral ratio, already for the factor of 3, the influence of non-linear soil behaviour is greatly reduced, however, we observe some minor effects (i.e. reduction of amplification at high frequency and increase at low frequency) even for input ground motion divided by a factor of 10. We suspect that there is a threshold of the amplitude of the input ground motion for which the non-linear response becomes significant and then we observe a kind of saturation i.e. increasing the amplitude does not have a big effect. Presented experiments are only the preliminary study of the influence of the amplitude of the input ground motion on the impact of the non-linearity; hence, the conclusions are not definitive. Much more investigations have to be done, for instance, the results in Figure 26 are only for one input ground motion and for a different seismic zone than the results in Figure 25, so they cannot be compared. In the next step, we plan to test several magnitude-distance scenarios to find the approximate amplitude limit for which we start to observe significant non-linearity.
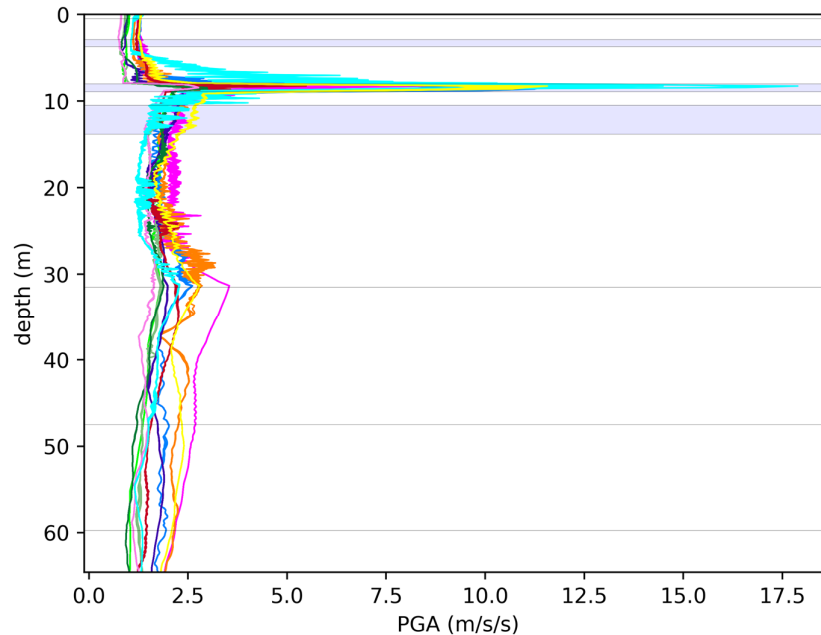


*Figure 23. PGA with depth for all ground motions in seismic zone Z2 (SIA261, 2020), one colour represents one input ground motion. The simulations were performed while changing dilatancy parameters for layer 2 and the resulting variability is represented here by the line thickness. Grey lines represent layers' borders while blue rectangular are liquefiable layers.*
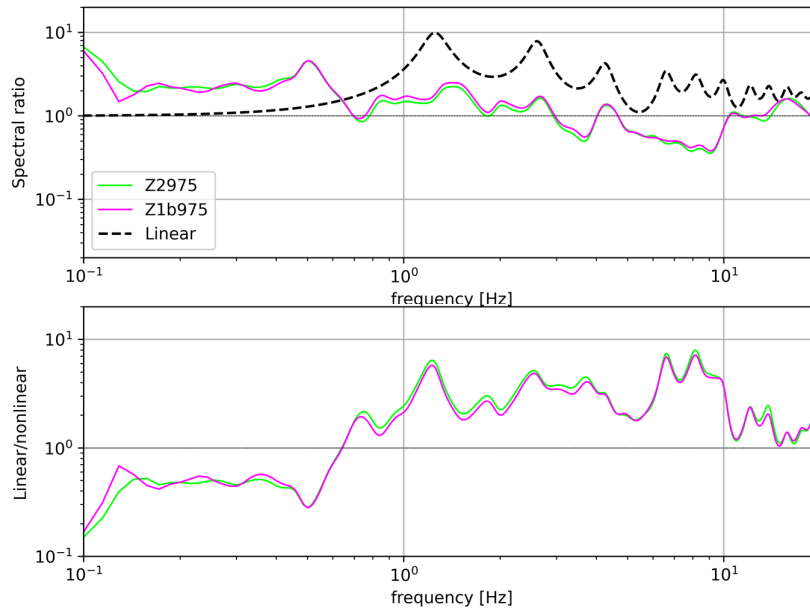
*Figure 24. The comparison of spectral ratios of the mean calculated over 11 scaled input ground motions for seismic zone Z1b and Z2 (SIA261, 2020). The black dashed line in the top plot is the linear response.*



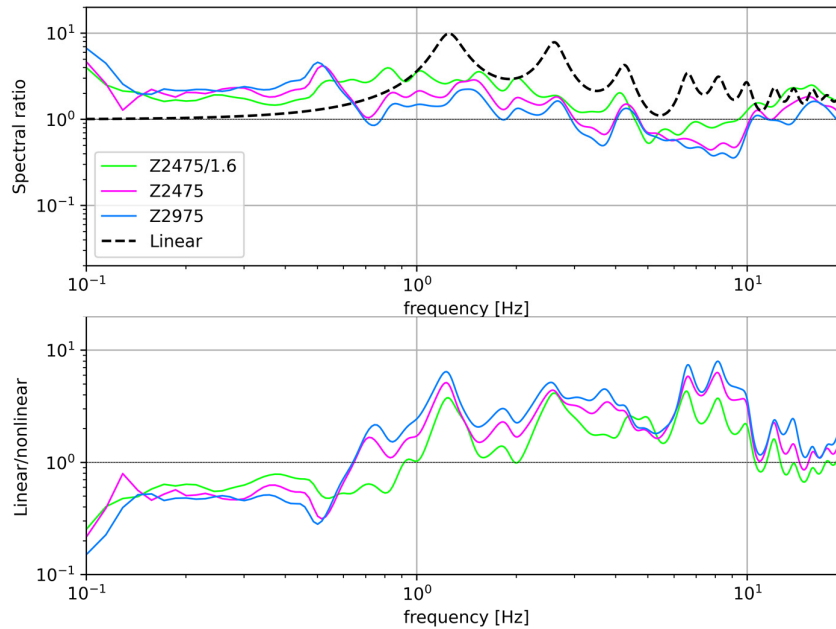*Figure 25. The comparison of spectral ratios of the mean calculated over 11 scaled input ground motions for seismic zone Z2 (SIA261, 2020) for return periods of about 975 and 475 years as well as for input ground motions for a return period of about 475 divided by 1.6 that approximates the input ground motions representing the uniform hazard spectrum. The black dashed line in the top plot is the linear response.*
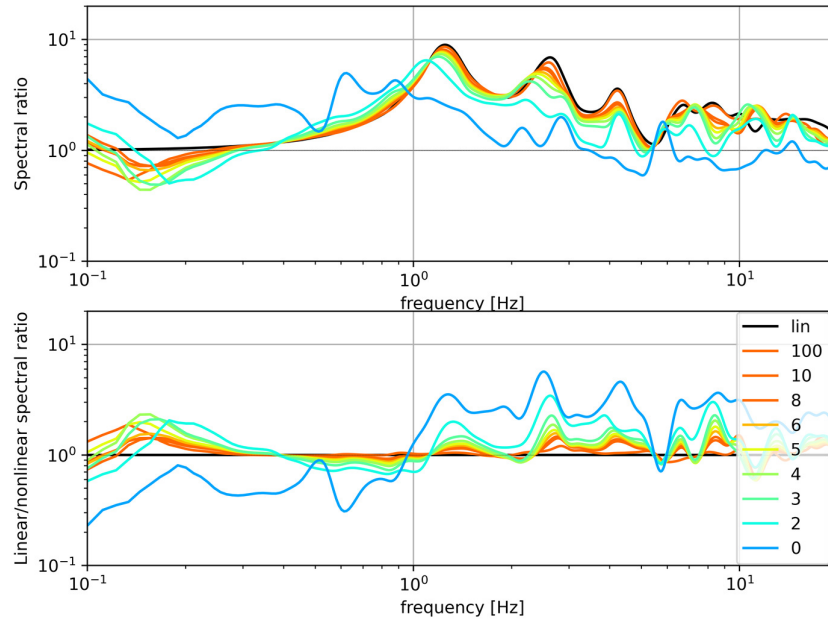
*Figure 26. The comparison of spectral ratios for one input ground motion that was respectively divided by 2, 3 … and 100 as specified in the legend. The chosen input ground motion is for a seismic zone Z1b (SIA261, 2020) for a return period of about 975 years. The black line is the linear response.*

Because we apply surface ground motion at the bedrock depth, we divided the amplitude by a factor of 2, however, in the next step of our analysis, we want to investigate and discuss if it is the correct solution and how it affects the results by applying deconvolved waveform as an input.

### 5.6 More on the influence of dilatancy parameters

We test the influence of each dilatancy parameter on pore pressure development in order to better understand their significance and illustrate their impact. We simulated the stress-controlled experiment by changing separately each of the dilatancy parameters but using the same CSR values repeating the simulations for several CSRs.

With the increasing value of $p_1$, more time and simultaneously more stress cycles are required before reaching liquefaction (Figure 27). The slope of the pore pressure curve at the initial phase is lower and less linear for high values of $p_1$, simultaneously; the strong oscillations of the curve start later. In the final phase of the pore pressure build-up is independent of $p_1$. On the contrary, more time for reaching liquefaction is required for low $p_2$ values (Figure 28). However, the increase of needed time is not linear, for very low values of $p_2$, the number of required stress cycles is non-proportionally high. While the slope in the initial phase is not influenced by $p_2$, with increasing values of $p_2$, the slope in the final phase increases, in addition, pore pressure reaches higher values. $w_1$ influences the pore pressure curve in the initial and final phase (Figure 29) – the lower $w_1$, the fastest pore pressure build-up in both phases. Finally, with the increasing value of threshold limit parameter $c_1$ (Figure 30), the angle of the initial slope is lower; however, it does not influence the bending of the pore pressure curve as $p_1$ and $w_1$. However, for very high values of $c_1$, we observe the influence on the curvature as well.

*Figure 27. The influence of dilatancy parameter $p_1$ on pore pressure development during a simulated stress-controlled experiment for CSR=0.15. Other parameters are listed at the top.*
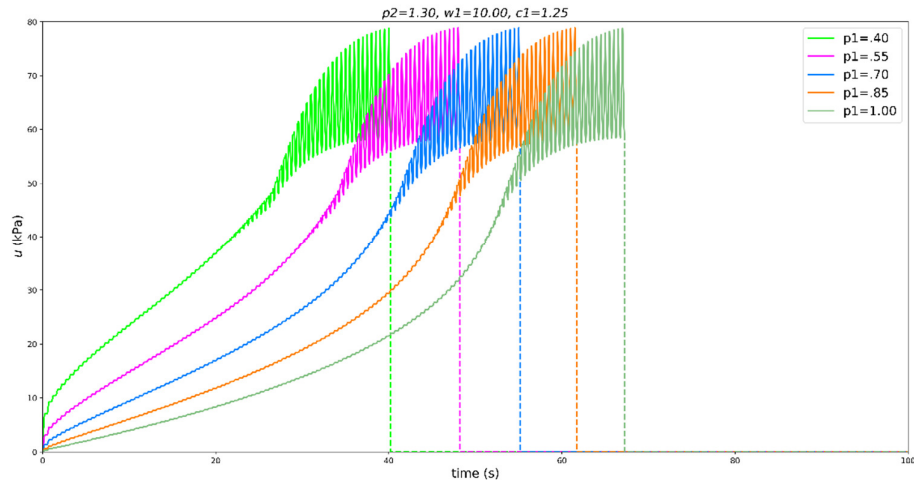


*Figure 28. The influence of dilatancy parameter $p_2$ on pore pressure development during a simulated stress-controlled experiment for CSR=0.21. Other parameters are listed at the top.*

All the presented examples are very relatively low CSR values (between 0.21 – 0.13) where pore pressure development is slow. For very high CSR values (>0.3), the differences depending on using different dilatancy parameters are not significant. The number of stress cycles needed to reach the liquefaction (i.e. 2.5% of strain) is very low and pore pressure excess build-up is almost immediate, so the impact of each dilatancy parameter is small. On the other hand, for very low CSR (<0.1) when the number of required stress cycles is high, the liquefaction is not reached within the maximum time for simulation, or in some cases, the simulation fails. Hence, for inversion of dilatancy parameters, we should put focus on intermediate CSR because too high and too low do not help in constraining the values of dilatancy parameters.

*Figure 29. The influence of dilatancy parameter $w_1$ on pore pressure development during a simulated stress-controlled experiment for CSR=0.17. Other parameters are listed at the top.*
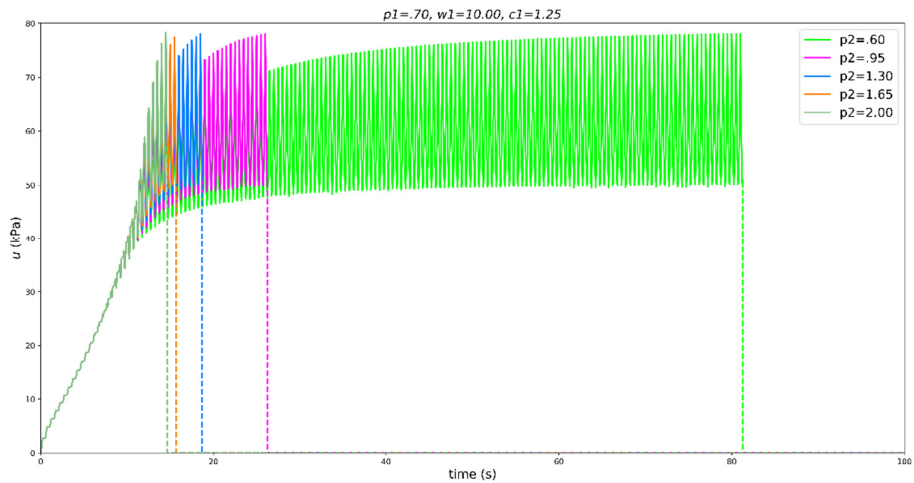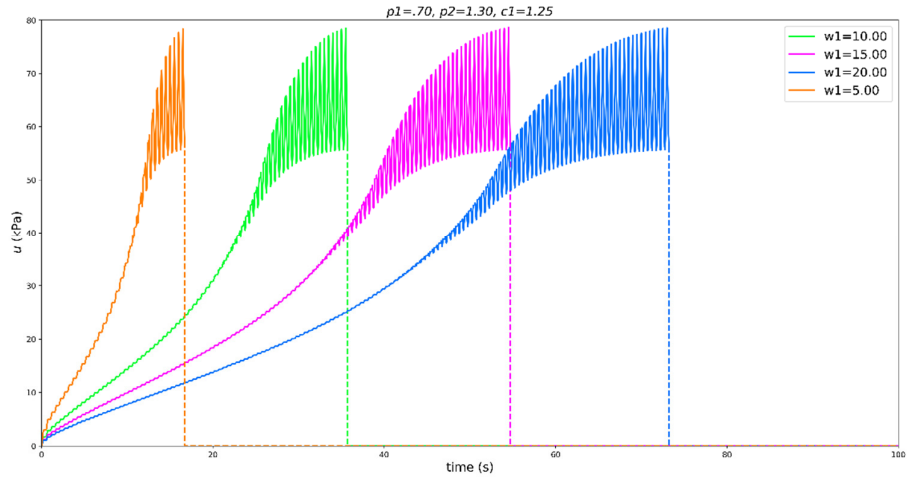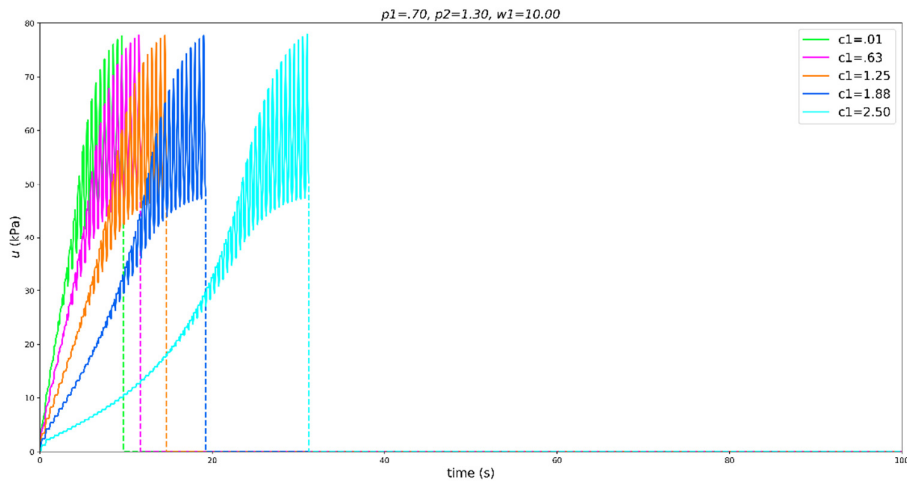


*Figure 30. The influence of dilatancy parameter $c_1$ on pore pressure development during a simulated stress-controlled experiment for CSR=0.23. Other parameters are listed at the top.*

As shown in chapter 5.4, the influence of changing dilatancy parameters on simulated wave propagation is minor for SLUW, however, it was investigated only using one site with relatively thin sandy layers and small variability of sets of dilatancy parameters. Hence, we experiment using the same soil profile but creating random 30 sets of dilatancy parameters for layer 1 and layer 2 within given limits (Table 3), either randomizing one or all parameters. In the first case, the rest of the parameters is the best set for a given layer (Table 3). All presented results are for one ground motion for seismic zone Z1b (SIA261, 2020).

The results do not depend significantly on the $p_1$ value. The variability for surface response spectra and non-linear spectral ratios are negligible; however, for spectral ratios, some minor variability is visible at low frequencies. Some impact of changing the $p_1$ value is observed for PGA at some depths, especially for the main peak whose value varies between about 2 and 5 m/s$^2$. With increasing $p_2$, we observe a gradual decrease of SA within the range between 0.25 and 2 s (Figure 31), reaching non-proportionally low values for very high $p_2$. For very short

periods (< 0.1 s) on the other hand, we observe an increase for high $p_2$ values. A quite high variability can be seen for spectral ratios with an increase of the amplitude of non-linear response with increasing $p_2$ at low frequencies, especially for very high values of $p_2$ (Figure 32). The maximum value of PGA for the profile can reach even 20 m/s$^2$ for low $p_2$, however, variability outside the main peak is not significant. We observe a significant decrease of SA for very low $w_1$ in the range between 0.5 and 2 s (Figure 33), while for very short periods (< 0.1 s), we see an increase of SA for very low $w_1$. Nevertheless, for intermediate and high values of $w_1$, there is no significant variability. The same is observed for spectral ratios, where the majority of the curves have similar values with a few outliers for low $w_1$ (Figure 34) causing the increase of non-linear response below 0.8 Hz and decrease between 0.8 and 2 Hz. Similarly for PGA values (Figure 35) - only low $w_1$ values influence the profile, especially by increasing significantly the peak value (even up to 18 m/s$^2$). When considering changing the value of $c_1$ for layer 2, we observe a slight gradual increase of SA (between 3.4 to 3.9 m/s$^2$ at the main peak) with increasing $c_1$, while there is almost no effect when testing for layer 1. Some variability can be seen for spectral ratios but no clear pattern is noticed (Figure 36). For PGA values, a significant increase at the main peak is observed (up to 16 m/s$^2$) for high $c_1$ for layer 2, on contrary for layer 1, a slight decrease is observed with increasing $c_1$.



*Figure 31. The variability of resulting response spectra depending on dilatancy parameter $p_2$ for layer 2 for one of the ground motions i seismic zone Z1b (SIA261, 2020), where red is the set with the lowest $p_2$ and yellow with the highest $p_2$ out of the set. The black dashed line shows the elastic response spectrum for soil class D and building importance class III in seismic zone Z2 (SIA261, 2020). The dotted black line is a response spectrum for the rock site and the black solid line is the resulting response spectrum if the linear viscoelastic response is simulated.*

*Figure 32. The variability of the resulting non-linear spectral ratio (top plot) and linear/non-linear ratio (bottom plot) depending on dilatancy parameter $p_2$ for layer 2 for one of the ground motions i seismic zone Z1b (SIA261, 2020), where red is the set with the lowest $p_2$ and yellow with the highest $p_2$ out of the set. The black line in the top plot represents the linear response.*
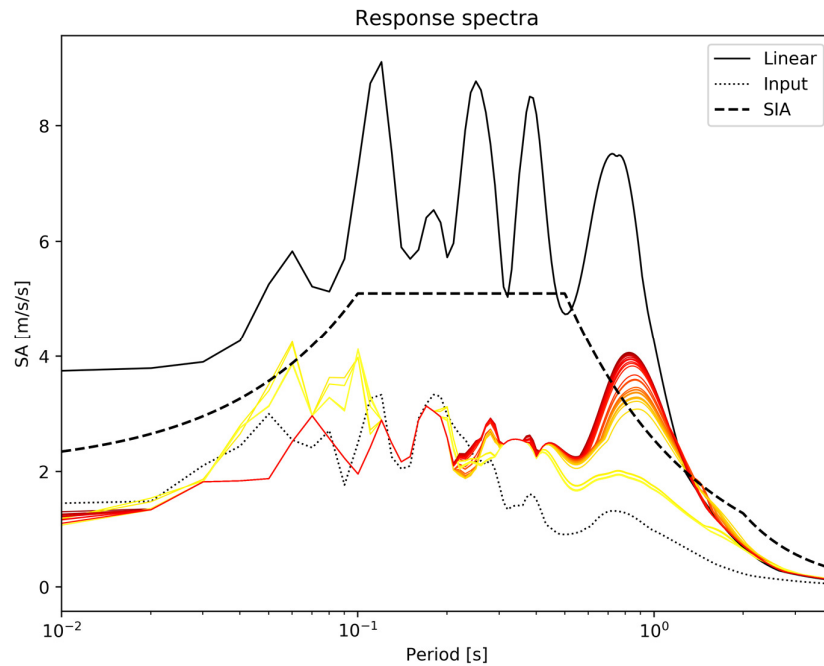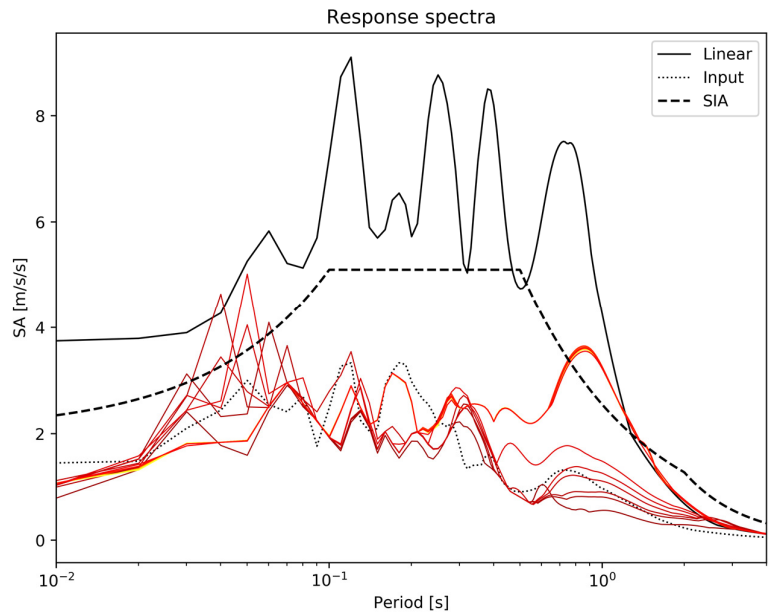


*Figure 33. The variability of resulting response spectra depending on dilatancy parameter $w_1$ for layer 1 for one of the ground motions i seismic zone Z1b (SIA261, 2020), where red is the set with the lowest $w_1$ and yellow with the highest $w_1$ out of the set. The black dashed line shows the elastic response spectrum for soil class D and building importance class III in seismic zone Z2 (SIA261, 2020). The dotted black line is a response spectrum for the rock site and the black solid line is the resulting response spectrum if the linear viscoelastic response is simulated.*
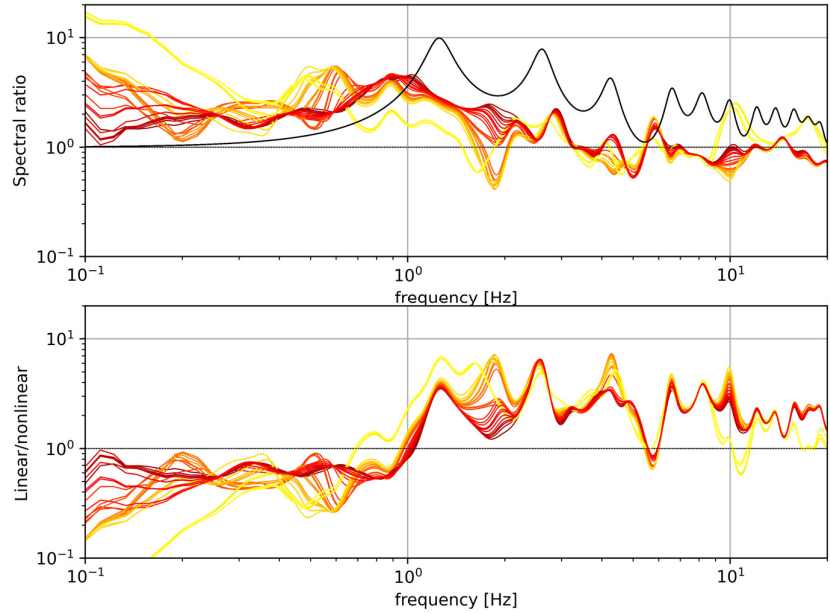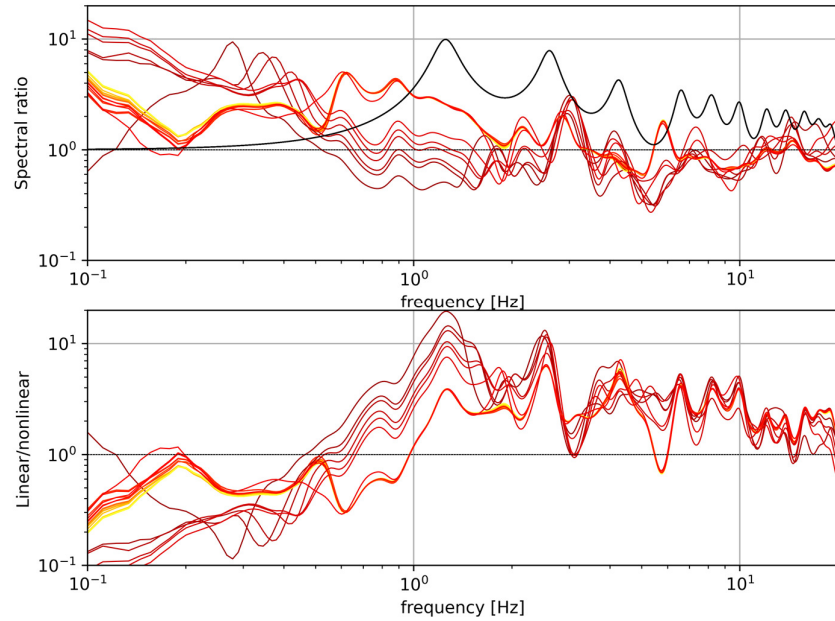
*Figure 34. The variability of the resulting non-linear spectral ratio (top plot) and linear/non-linear ratio (bottom plot) depending on dilatancy parameter $w_1$ for layer 1 for one of the ground motions i seismic zone Z1b (SIA261, 2020), where red is the set with the lowest $w_1$ and yellow with the highest $w_1$ out of the set. The black line in the top plot represents the linear response.*
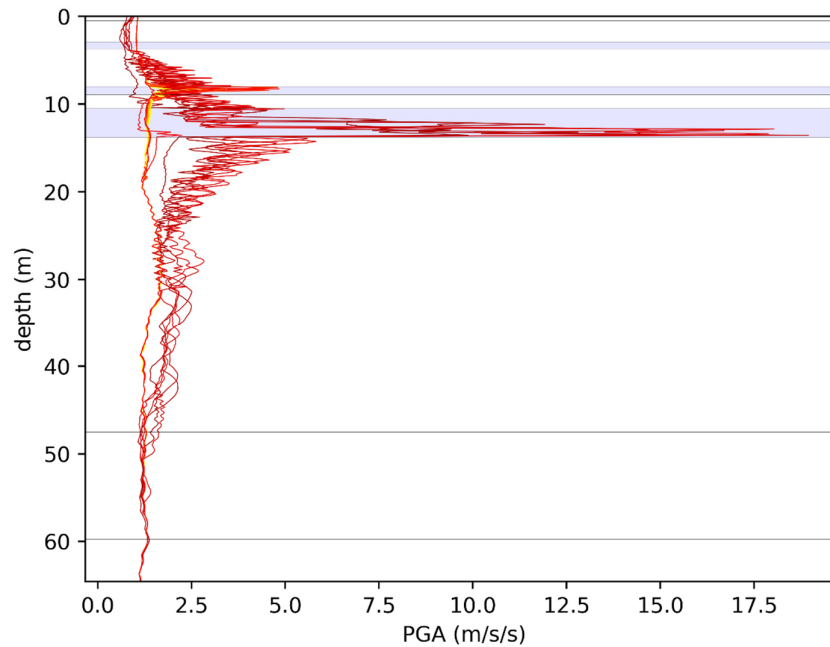


*Figure 35. The variability of resulting PGA with depth depending on dilatancy parameter $w_1$ for layer 1 for one of the ground motions i seismic zone Z1b (SIA261, 2020), where red is the set with the lowest $w_1$ and yellow with the highest $w_1$ out of the set. Grey lines represent layers' borders while blue rectangular are liquefiable layers.*

*Figure 36. The variability of the resulting non-linear spectral ratio (top plot) and linear/non-linear ratio (bottom plot) depending on dilatancy parameter $c_1$ for layer 2 for one of the ground motions i seismic zone Z1b (SIA261, 2020), where red is the set with the lowest $c_1$ and yellow with the highest $c_1$ out of the set. The black line in the top plot represents the linear response.*
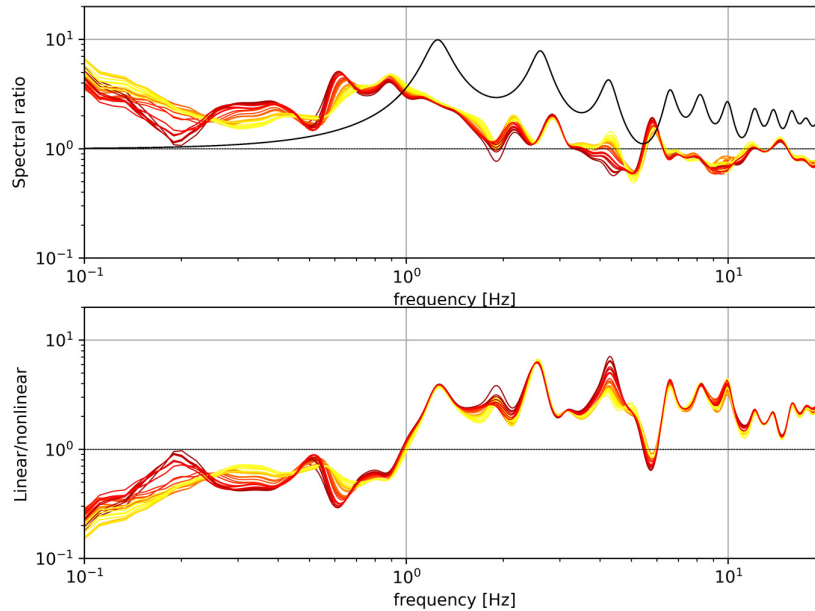
In another experiment, we use 30 completely random sets of dilatancy parameters. For surface response spectra, the differences are small, the results are more variable only for a few sets; however, they always show lower SA (Figure 37). Similar observations about variability are made for spectral ratios (Figure 38) and PGA, however, for the latter; the outliers can reach very high values, even up to 25 m/s$^2$.

To summarize, the least influence is visible for changing $p_1$, while the highest impact is observed for $p_2$. For $w_1$ and completely randomized sets, the results are not so diverse but we see outliers with very different values. We do expect higher variability for a completely randomized set; however, it appears that for most of the combinations the effect is not significant, less than influence for individual parameters. We suspect that one of the reasons is the thinness of the considered layers in which only exceptional values of dilatancy parameters have a significant impact on the whole profile. Another reason is that the effect of the parameters may cancel each other in completely randomized sets, while if only one parameter is changing, the effect is more pronounced. We observe the differences in the results depending if the parameters for layer 1 or layer 2 are randomized, but we do not observe any clear tendencies. Sometimes more effect is seen if we investigate layer 1 because it is thicker, however, it is not a rule. For some values like $c_1$, we see different behaviour depending on the considered layer as well as the different intensity of the variability, hence, what is important is the combination of the parameters not only the changes of the individual parameter. Another issue is that not all the possible combinations should be tested because they do not occur normally in real case studies.
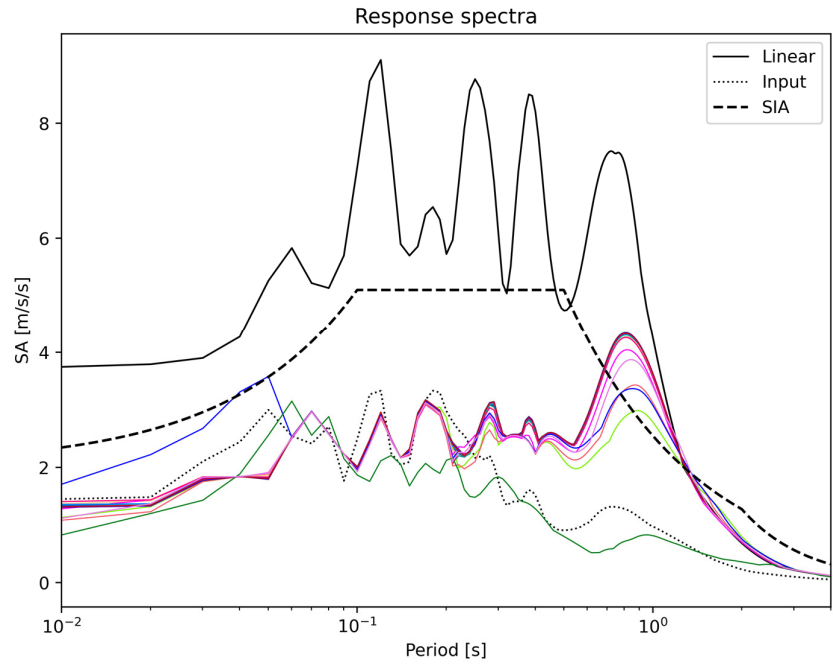
*Figure 37. The variability of resulting response spectra depending on the random set of dilatancy parameters for layer 2 for one of the ground motions i seismic zone Z1b (SIA261, 2020). Colors are assigned randomly. The black dashed line shows the elastic response spectrum for soil class D and building importance class III in seismic zone Z2 (SIA261, 2020). The dotted black line is a response spectrum for the rock site and the black solid line is the resulting response spectrum if the linear viscoelastic response is simulated.*



*Figure 38. The variability of the resulting non-linear spectral ratio (top plot) and linear/non-linear ratio (bottom plot) depending on the random set of dilatancy parameters for layer 2 for one of the ground motions i seismic zone Z1b (SIA261, 2020). Colors are assigned randomly. The black line in the top plot represents the linear response.*

Last but not least, we tested the influence of the precision of the used set of dilatancy parameters. Usually, in literature (e.g. Iai et al., 1990), the dilatancy parameters are given with one digit precision but in our analysis, we use two digits. As an experiment, we chose the 30 best unique sets of dilatancy parameters but this time with one-digit precision, which made the sets more spread out. While for layer 1, the differences are again almost invisible because the inversion results do not give diverse sets of parameters; for layer 2, we see higher variability. However, it is still not significant; the maximum value of SA varies between 3.4 and 3.8 m/s$^2$. For spectral ratio, we see some variability at low frequencies (Figure 39). Nevertheless, PGA values at the main peak vary between 3 and almost 18 m/s$^2$.
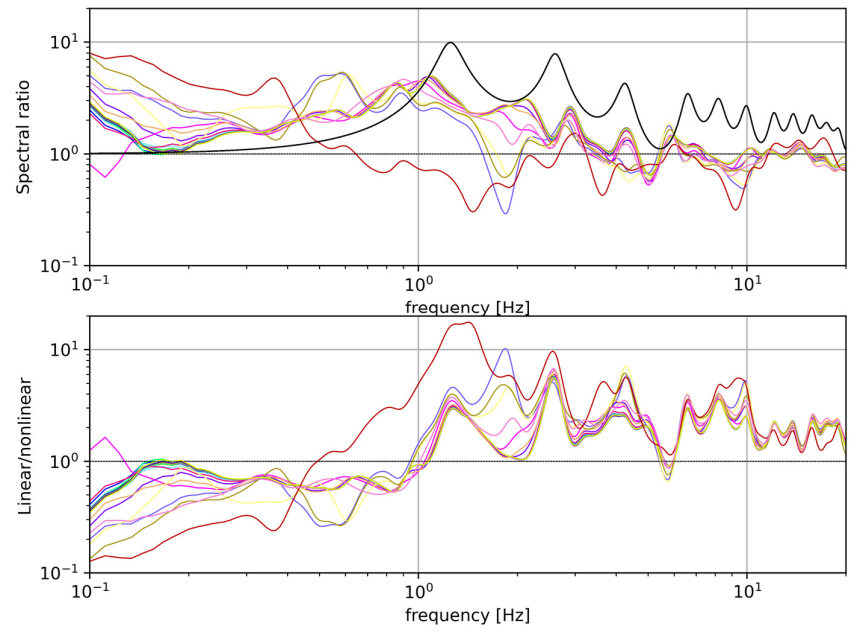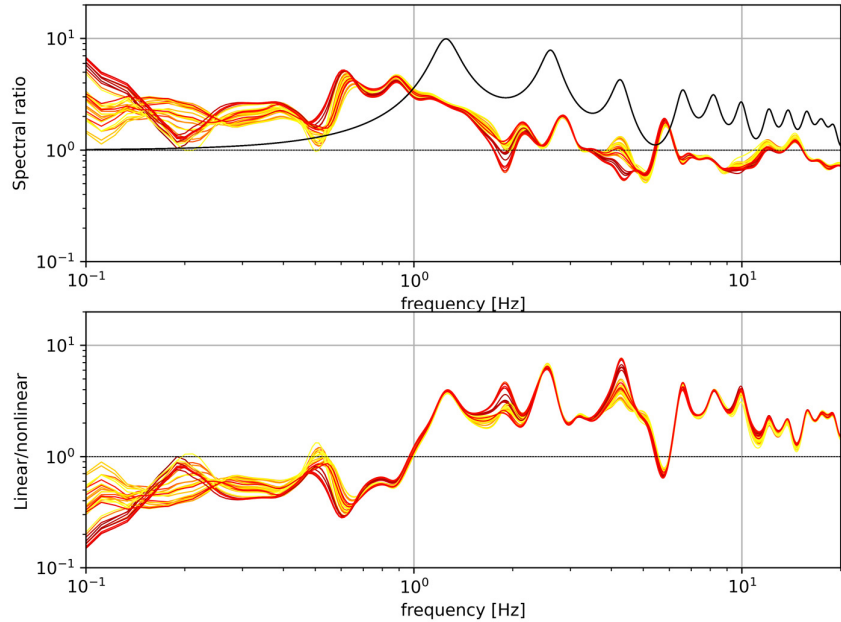


*Figure 39. The variability of the resulting non-linear spectral ratio (top plot) and linear/non-linear ratio (bottom plot) depending on the chosen set of dilatancy parameters for layer 2 for one of the ground motions for seismic zone Z1b (SIA261, 2020), where red is the set with the lowest and yellow with the highest misfit out of the set. The considered sets of dilatancy parameters have only one digit. The black line in the top plot represents the linear response.*

## 5.7 Inversion testing

The inversion procedure by Roten (2014) to obtain dilatancy parameters from CPT was never extensively tested and applied in a real case example. We tested the whole inversion process, investigated several factors affecting the results as well as performed preliminary sensitivity testing of several input parameters (e.g. Poisson ratio, $K_0$, $V_s$, $\rho$); however, more work has to be done to fully assess their impact. We created synthetic examples of the LRC curves with a known set of dilatancy parameters to test how well the procedure can reproduce the model. In addition, we performed tests on a real case study (SLUW). Moreover, we tested some technical aspects of the inversion process by examining among others the influence of the number and stress range of the simulated stress-controlled experiments, different model search ranges, and more and less explorative inversion procedure. Last but not least, some attempts of exploring the impact of the applied forward model have been done.

### 5.7.1 Synthetic LRC curves

In order to test if the inversion algorithm is performing well, we created several synthetic LRC curves using input parameters for either layers 1 and 2 and a known set of dilatancy parameters. When using the input data for layer 1, in the majority of the cases, we are able to retrieve the values of dilatancy parameters with good precision (up to 1 or even 2 digits) using the presented inversion. However, for synthetic LRC curves generated using data for layer 2, the problem often is too non-unique, and the initial set of dilatancy parameters is not always found. Another observation is that in case the input LRC curve is not a regular exponential curve (i.e. the one generated from $CRR_{7.5}$), in many cases, it was possible to retrieve the same set of dilatancy parameters.

### 5.7.2 Different datasets

For the shallow part of the SLUW profile, we generated 3 distinct datasets: the first one based only on CPT, the second using $V_s$ and density directly from the downhole seismic experiment (EXT, Figure 6), and finally smoothed S-wave and density profiles from downhole (EXT2, Figure 13). For all layers, the difference between the original and smoothed $V_s$ profile is small in terms of misfit, for layer 1 is smaller for the smoother version, and for layers 2 and 3 is slightly higher, however, for a matter of consistency, we used the smoothed version for obtaining final results (Table 3). For layer 1, the dataset consisting only of CPT, shows the highest misfit (Figure 40), in the case of layers 2 and 3 – there is no convergence – we cannot find a model that fits the data. Independent on the dataset, the results show similar trends, for layers 1 and 3 – both $p_1$ and $p_2$ approach the maximum limit of the search range, however, showing some local minima, while $w_1$ and especially $c_1$ approach one value. For layer 2, we observe good convergence for $w_1$ and $c_1$, while $p_1$ and $p_2$ show several minima, especially $p_1$ which covers quite uniformly the whole model space.

### 5.7.3 Forward model

In the initial forward model that simulates the stress-controlled experiment, stress and strain are scaled in order to control damping. We test the forward model with disabled damping control. For layer 2, we do not observe any significant difference, resulting values of $p_2$, $w_1$ and $c_1$ are similar independently of chosen forward model, and $p_1$ takes a different value in every run because of the non-uniqueness of the problem. However, for layer 1, we see less effect of $p_1$ and $p_2$ approaching the maximum limit of the search range. The algorithm finds also other minima. Hence, we prefer the forward model without damping control. We plan to test another forward model based on Iwan's elastoplastic model (Oral, 2016); it is still ongoing work.

### 5.7.4 Search range limits

One of the most important factors that we tested is the limits of the search range of the model space. As shown in Figure 41, the results are very sensitive to the choice of the search range in the case of layer 1, because $p_2$ and especially $p_1$ always approach the maximum of the model space. However, we cannot assess its general importance using only the example of SLUW, it needs to be tested every time, especially because for layer 2, we do not observe much influence of expanding the search range.

For layer 1, we performed also an experiment when we expand the upper limits of the search range drastically for each parameter (Table 5). The resulting $p_2$ reaches unrealistically high values (

Table 6), while other parameters remain within realistic limits. It shows the importance of constraining the limit of the search. Even though $p_2$ which is equal to 90 can explain data the best from a mathematical point of view but it is much outside the ranges reported in the literature (Iai et al., 1990). The most realistic search ranges according to literature and our experience are given in Table 3. Those conclusions are supported by an experiment using a few synthetic LRC curves – we were able to get close to the model values with a constrained search range, however, for an extended search range, the results tend to worsen significantly.
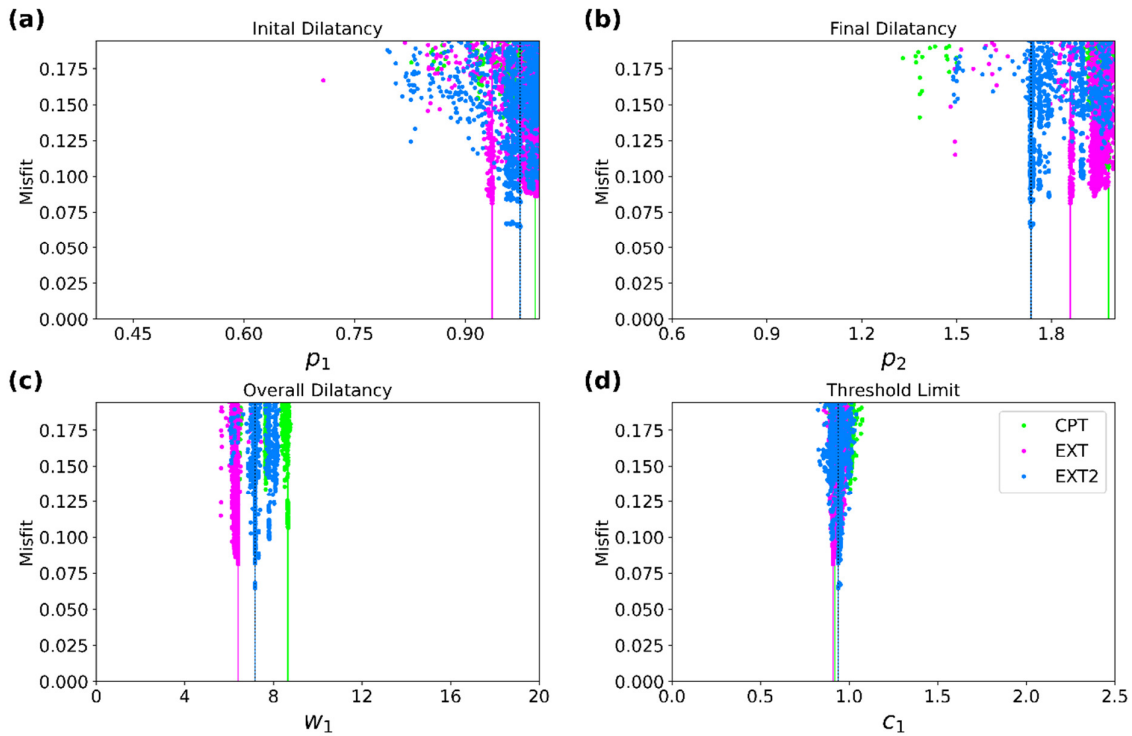


*Figure 40. The inversion results for layer 1 depending on the dataset (based on CPT, downhole seismic profile – EXT, and smoothed downhole seismic profile – EXT2).*

### 5.7.5 Inversion parameters

When changing the inversion procedure from more exploitative to more explorative, the model space is searched more extensively. We tested it using several examples. Considering the non-unique character of the problem, we decide that the most optimal solution is to switch the inversion process to very explorative to find several local minima. The chosen parameters are shown in Table 4. However, we need to keep in mind the computational and time constraints.
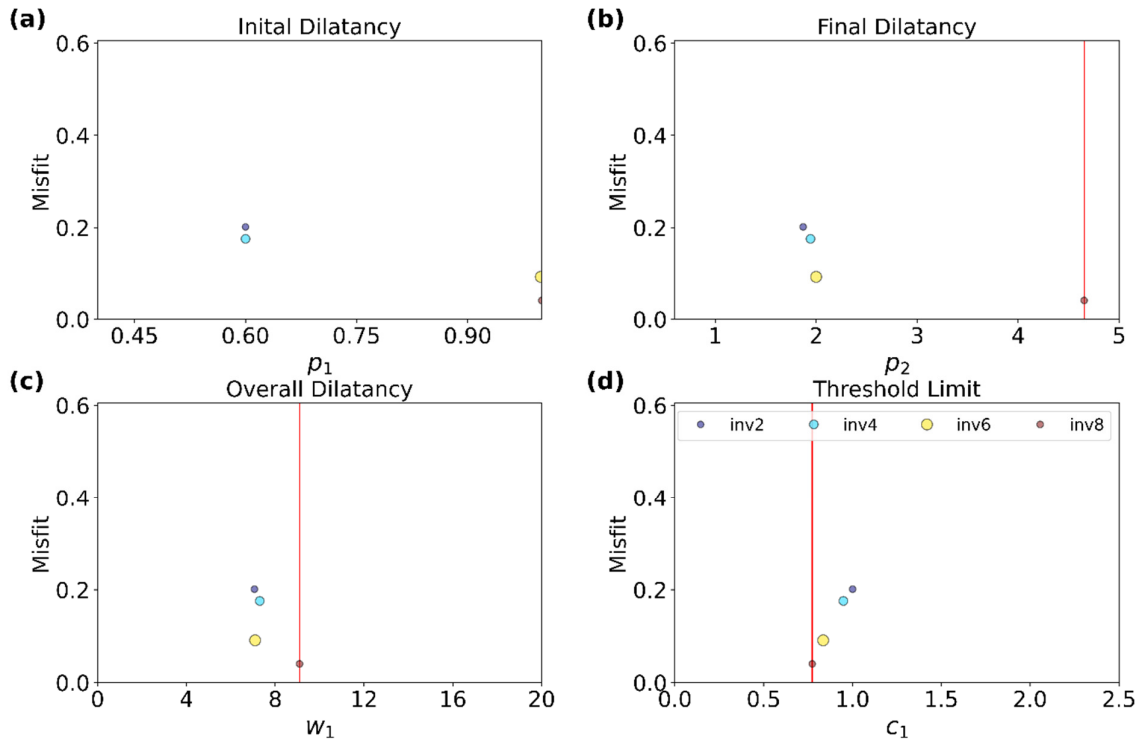
*Figure 41. The influence of changing the inversion search range (Table 5) for layer 1. Circles show the best results of each of the run and the red line show the best set out of considered runs.*

*Table 5. Inversion search ranges for experiments shown in Figure 41 (inv2 to inv8) and for investigating the effect of an unrealistically broad search range.*

| Inversion | P1 | P2 | W1 | C1 |
|---|---|---|---|---|
| Inv2 | 0.4 – 0.6 | 0.6 – 2.0 | 0-20 | 1 |
| Inv4 | 0.4 – 0.6 | 0.6 – 2.0 | 0-20 | 0-2.5 |
| Inv6 | 0.4 – 1.0 | 0.6 – 2.0 | 0-20 | 0-2.5 |
| Inv8 | 0.4 – 1.0 | 0.6 – 5.0 | 0-20 | 0-2.5 |
| Maximum search | 0.1 – 20.0 | 0.1 – 100 | 0-500 | 0-20 |

*Table 6. The results for the experiment where the search range was unrealistically broad (Table 5) using a forward model with and without damping control.*

| Dilatancy parameter | Damping control | No damping control |
|---|---|---|
| $p_1$ | 0.31 | 4.55 |
| $p_2$ | 89.16 | 46.12 |
| $w_1$ | 4.54 | 1.60 |
| $S_1$ | 0.01 | 0.01 |
| $c_1$ | 0.64 | 0.78 |

### 5.7.6    Influence of the LRC curve

We investigated the influence of using a smaller number of stress-controlled simulations, reducing using 14 stress levels to 4-5 but keeping the same range of CSR values. We conclude that even though the results are similar and the misfit is much lower (Figure 42), the searched model space is smaller introducing the possibility of being stuck in a local minimum.



*Figure 42. In the upper panel: results of inversion and input and simulated LCR curves when simulations for 14 CSR values were performed; lower panel: for 4 CSR values. The results are for layer 1.*

In another experiment, we tested the impact of using a shorter LRC curve (CSR>0.14, Figure 43). While for layer 1, the results are not much influenced and we cannot make any clear conclusions about tendencies, for layer 2, it has a significant impact because the curve was more extended for low CSR values. While using the whole LRC curve, only the $p_1$ value is not well-constrained, for reduced CSR, other parameters are also much less constrained, showing several minima. Tests using synthetic examples do not show much difference - if we were able to retrieve the correct set of parameters using the whole CSR curve, removing low CSR values does not change the results significantly. However, if the correct set was not found using the whole curve, using a shorter LRC curve does not improve the result.
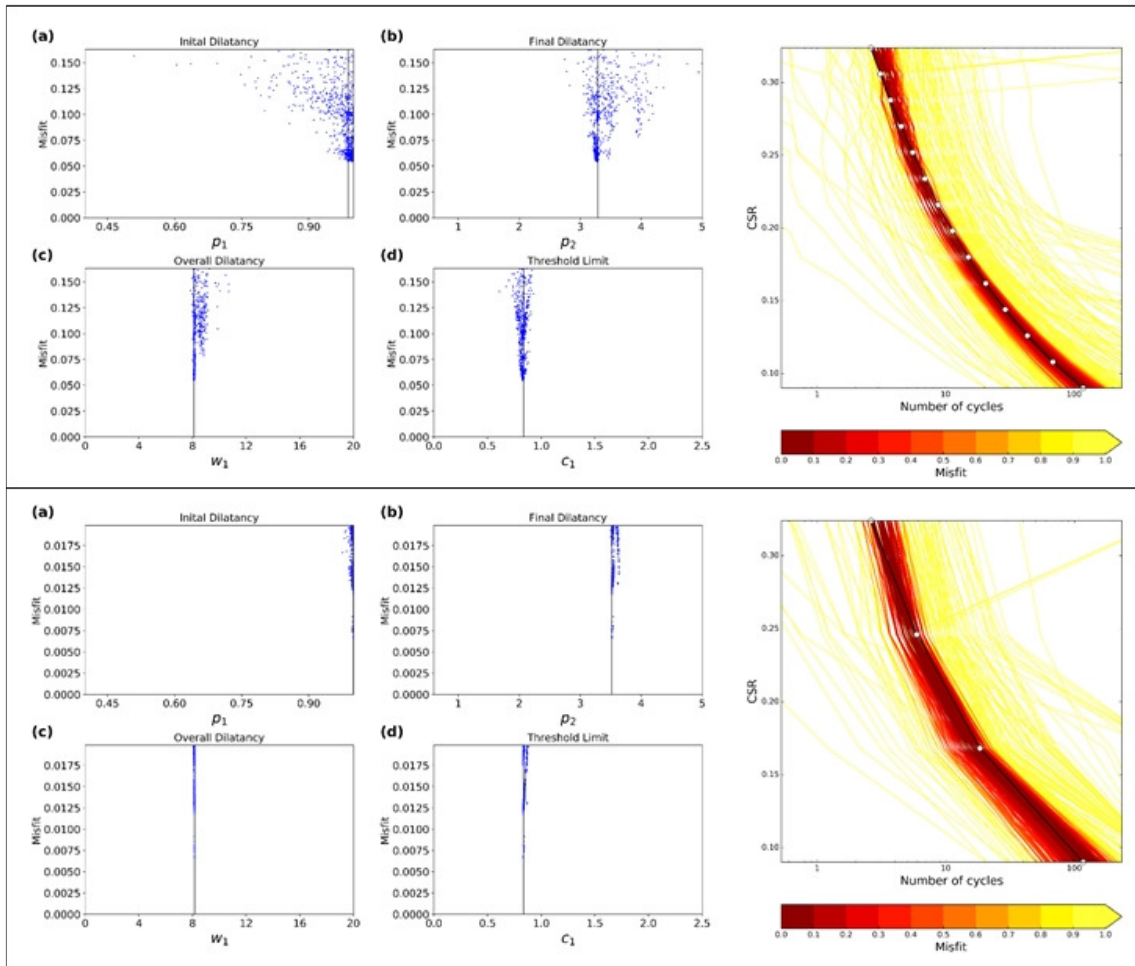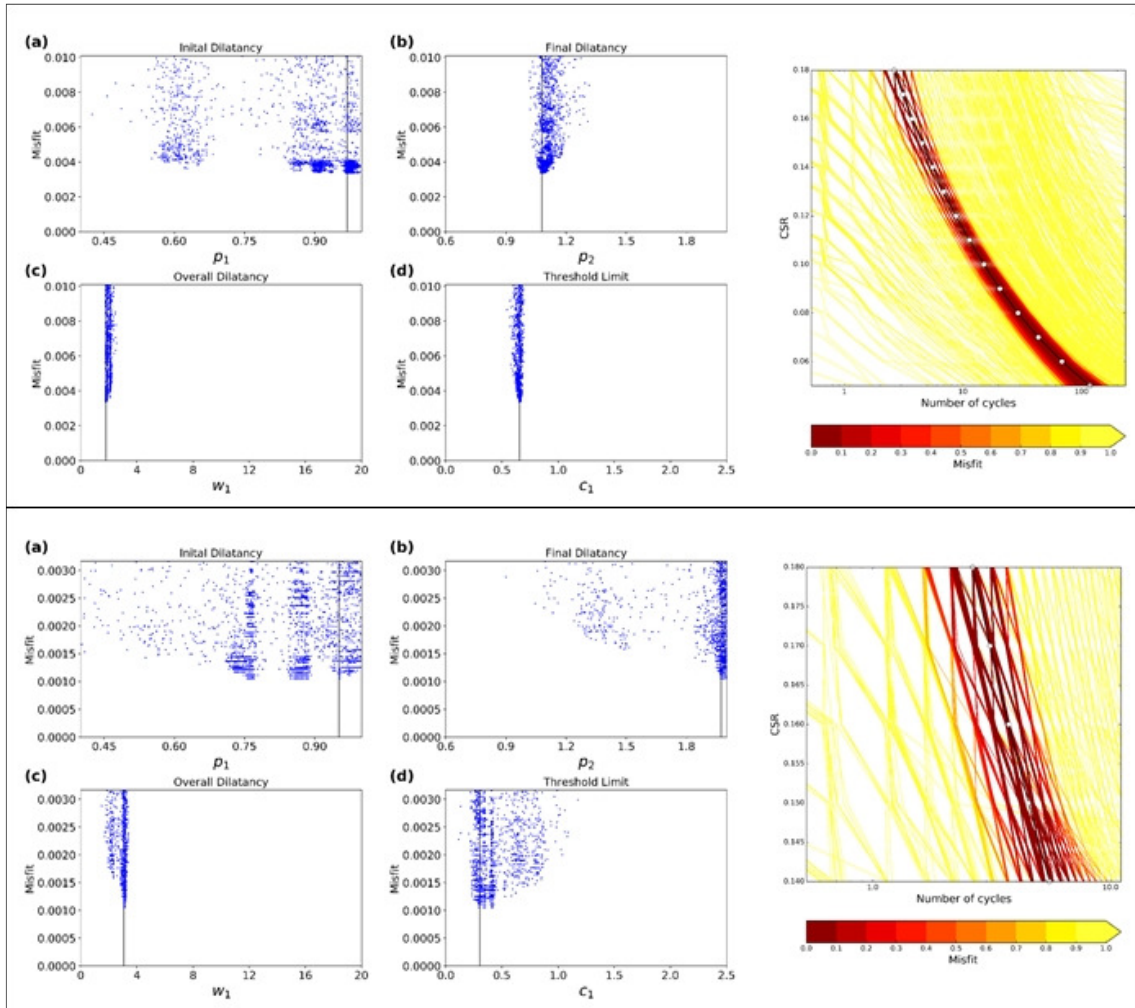
*Figure 43. In the upper panel: results of inversion and input and simulated LCR curves when simulations for 14 CSR values were performed; lower panel: for CSR values higher than 0.14. The results are for layer 2.*

Lastly, we used only CSR values from 0.4 to 0.6 expanding the previously used curve (CSR<0.4). First of all, for high values of CSR (CSR>0.4), the simulations often fail; secondly, the results are much worse. Hence, according to our observation and literature recommendation (Roten, 2014), the maximum LRC curve should not exceed 0.4. For higher values that are equivalent to very strong earthquakes, simulated strain exceeds 2.5% almost immediately and pore pressure build-up is very fast. We showed that in such a case, the pore pressure development is almost the same independently on the set of dilatancy parameters, especially when it comes to parameters responsible for the initial phase ($p_1$, $w_1$, $c_1$).

### 5.7.7 Input parameters

We preliminarily investigated the influence of several input parameters on the results using data for layer 1 and layer 2. Changing the Poisson ratio from 0.33 to 0.45 does not influence the results for layer 2, while for layer 1, increasing the Poisson ratio causes $p_1$ and $p_2$ to approach even more the maximum of the model range limits. The results are quite sensitive to changes in $V_s$ and $\rho$; however, no clear pattern was observed. The results for layer 2 are

not influenced if $K_0$ is increased to 1, however changing to $K_0=0.5$, the results are significantly affected, while for layer 1, the results are slightly affected by both changing to $K_0=1$ and $K_0=0.5$.

### 5.7.8   Summary and future work

We think that the most important parameter while performing the inversion using the procedure by Roten, (2014) is the search range limit for the model space. It is important to maintain the explorative character of the inversion process as well as use the broad range of stress levels used for simulations but not exceeding CSR=0.4. However, the performed analysis does not give us definite answers about the influence of all the tested parameters, much more extensive investigation needs to be done using many case studies and synthetic examples to fully understand the impact of all the given aspects. If possible, the results should be verified using laboratory data but a good approach would be also to generate a big number of experiments and analyze those using statistical methods or machine learning. In our case, because of limited time, we investigate different influencing factors using only a few examples. However, we are able to observe some trends and confirm that while constraining the model space, the procedure often gives realistic results. One of the observed problems is that for some datasets (e.g. layer 1 and layer 2 in our case study), the same parameters have a decisive or negligible effect, so performing preliminary tests for a given case study are recommended for future users. The considered inverse problem is non-linear and often non-unique; several sets of dilatancy parameters can explain the data similarly. Another issue that should be taken into account while performing the inversion is the fact that typically, the dilatancy parameters are determined using a sequential trial and error method (Iai et al., 1990). The individual dilatancy parameters should be calibrated one by one using different stress levels, while in our case – all are estimated simultaneously. In the future, the inversion procedure can be updated in order to consider it.

## 6.   Conclusions

The presented study is a preliminary analysis of non-linear site response in the city of Lucerne in central Switzerland which is located in a basin filled with unconsolidated saturated deposits. We show the results of 1D modelling of wave propagation at one selected site that is characterized by very low shear wave velocity in the shallow part (<300 m/s below 30 m), low fundamental resonance frequency $f_0$ (1.2 Hz), and high amplification factors (>10 at $f_0$). We calibrate the model parameters using mostly CPT data and shear wave velocity profile from the downhole seismic experiment. Soil geotechnical parameters were derived using empirical relations from CPT measurements; however, such equations provide only approximated values and involve significant uncertainty. Nevertheless, the comparison to a nearby borehole shows that CPT estimation can qualitatively approximate the site lithology, while shear wave velocity derived from CPT can be used only if the resolution of the S-wave profile from seismic is too low in the shallow part. Our analysis shows also the importance of testing the shear wave velocity profiles using 1D linear simulations and comparing them to empirical amplification functions if available in order to calibrate the 1D velocity profile.

Because we wanted to consider dilatancy and cyclic mobility for sandy water-saturated layers, we needed to estimate dilatancy parameters (Iai et al., 1990) for them. Since there is no

laboratory data available, we used the inversion procedure introduced by Roten, (2014) in which the LRC curve derived from CPT data is inverted using a simulation of a stress-controlled triaxial experiment with a liquefaction front model (Iai et al., 1990) as a forward model. Because the procedure was never fully tested, we investigated several aspects concluding that the procedure can be used as a tool for finding dilatancy parameters for non-linear soil behaviour studies instead of the often-used extensive trial and error method. Using synthetic examples, we showed that we are able to recover original sets of parameters in most of the cases, however, for some examples; the problem was too non-linear and non-unique. For real data, reasonable sets of dilatancy parameters were also found, however, the model space limits need to be constrained in many cases to avoid obtaining unrealistic values. Controlling the model space boundaries was found to be the most important factor affecting the inversion results. It is also important to calibrate the inversion algorithm to be explorative and search the model space extensively to avoid being stuck in local minima because of the non-uniqueness of the problem. In addition, optimally, several stress-controlled experiments should be simulated for different stress levels, however, limiting the LRC curve to CSR<0.4 because, for higher stress levels, the pore pressure excess build-up is almost immediate and the dilatancy parameters cannot be well constrained. We investigated also the influence of some input parameters showing that even though their effect is not significant and we cannot find a consistent pattern, it should be considered when estimating the uncertainty. Nevertheless, to assess fully the impact of the input parameters, more investigations including a statistical number of sites need to be performed.

We performed the simulations using 11 scaled waveforms showing significant variability depending on input ground motion. From all tested influencing factors, the input ground motions are affecting the results the most. It is an important observation when it comes to the predictability of the non-linear response for different scenarios – the outcome is non-linearly dependent on the input. When comparing the linear and non-linear site response, we observe strong non-linear effects in the case of Lucerne for the input ground motion for a return period of about 975 years which is however very extreme and conservative scenario. Below 1 Hz, the non-linear response is much higher than linear, while above 1 Hz, the non-linear case is not only lower than linear but is lower than the input ground motion indicating strong de-amplification and damping of the ground motion. Nevertheless, the high impact of the non-linearity in the high frequency can be connected as well to the fact that only shallow layers (<30 m) are considered non-linear in our model. Even though the observed non-linearity is strong, the pore pressure changes in the considered thin layers may not produce enough effect. We may observe more pronounced non-linear effects at other sites in the Lucerne. Moreover, the frequency content of input ground motion may not match the fundamental frequency of the soil reducing the non-linear effects. We suspect that above some value of the amplitude of the input ground motion, we observe saturation of the response – it becomes independent of the amplitude as well as impedance contrast between rock and sediments, which needs to be further tested.

Because of the uncertainty of the input data and inversion process, we chose 30 sets of dilatancy parameters with the lowest misfit to investigate their influence. However, mostly because of the thinness of the sandy water-saturated, the effect is insignificant. We need an

experiment for the site where liquefiable-prone layers are much thicker to check if the influence would be greater. It will be done in the next step of our study. Nevertheless, we tested the effect of more diverse sets of dilatancy parameters by using randomized values. We showed that the results are mostly influenced by changing final dilatancy $p_2$ and in less extent overall dilatancy $w_1$, while threshold limit $c_1$ and especially initial dilatancy $p_1$ have a much less pronounced effect. Nevertheless, the variability is less than expected; however, the effect of dilatancy parameters cannot be ignored.

In the next step of our analysis, we will investigate another 1D site characterized by thick sandy saturated layers; however, the geology of the area is clearly 2D/3D, hence to better study the problem of non-linearity and liquefaction in Lucerne, we need to employ 2D or 3D models. We would like also to investigate the influence of the surface wave generated in the basin on pore pressure effects and liquefaction hazard.

## 7. Acknowledgments

## 8. References

Andrews, D. J. (1986). Objective Determination of Source Parameters and Similarity of Earthquakes of Different Size. In *Earthquake Source Mechanics* (Das, S., Boatwright, J., Scholz, C. H., Vol. 37, pp. 259–267). American Geophysical Union (AGU). https://doi.org/10.1029/GM037p0259

Baker, J. W., & Lee, C. (2018). An Improved Algorithm for Selecting Ground Motions to Match a Conditional Spectrum. *Journal of Earthquake Engineering*, *22*(4), 708–723. https://doi.org/10.1080/13632469.2016.1264334

Beresnev, I. A., & Wen, K.-L. (1996). Nonlinear soil response—A reality? *Bulletin of the Seismological Society of America*, *86*(6), 1964–1978.

Bergamo, P., Hammer, C., & Fäh, D. (2020). On the Relation between Empirical Amplification and Proxies Measured at Swiss and Japanese Stations: Systematic Regression Analysis and Neural Network Prediction of Amplification. *Bulletin of the Seismological Society of America*. https://doi.org/10.1785/0120200228

Bergamo, P., Hammer, C., & Fäh, D. (2021a). Correspondence between Site Amplification and Topographical, Geological Parameters: Collation of Data from Swiss and Japanese Stations, and Neural Networks-Based Prediction of Local Response. *Bulletin of the Seismological Society of America*. https://doi.org/10.1785/0120210225

Bergamo, P., Janusz, P., Panzera, F., Perron, V., Imtiaz, A., & Fäh, D. (2021b). *National and local site amplification models from the Earthquake Risk Model for Switzerland project*. 19th Swiss Geoscience Meeting, Geneva.

Bonilla, L. F. (2001). *NOAH: User's Manual*.

Bonilla, L. F., Archuleta, R., & Lavallée, D. (2005). Hysteretic and dilatant behavior of cohesionless soils and their effects on nonlinear site response: Field data observations and modeling. *Bulletin of the Seismological Society of America*, *95*, 2373–2395.

Bonilla, L. F., Guéguen, P., & Ben-Zion, Y. (2019). Monitoring Coseismic Temporal Changes of Shallow Material during Strong Ground Motion with Interferometry and Autocorrelation. *Bulletin of the Seismological Society of America*, *109*(1), 187–198. https://doi.org/10.1785/0120180092

Borcherdt, R. D. (1970). Effects of local geology on ground motion near San Francisco Bay. *Bulletin of the Seismological Society of America*, *60*(1), 29–61.

Boudghene Stambouli, A., Zendagui, D., Bard, P.-Y., & Derras, B. (2017). Deriving amplification factors from simple site parameters using generalized regression neural networks: Implications for relevant site proxies. *Earth, Planets and Space*, *69*(1), 99. https://doi.org/10.1186/s40623-017-0686-3

Brocher, T. (2007). Key elements of regional seismic velocity models for long period ground motion simulation. *Journal of Seismology*, *12*, 217–221. https://doi.org/10.1007/s10950-007-9061-3

Burjánek, J., Gassner-Stamm, G., Poggi, V., Moore, J. R., & Fäh, D. (2010). Ambient vibration analysis of an unstable mountain slope. *Geophysical Journal International*, *180*(2), 820–828. https://doi.org/10.1111/j.1365-246X.2009.04451.x

Chandra, J., Guéguen, P., & Bonilla, L. F. (2016). PGA-PGV/Vs considered as a stress–strain proxy for predicting nonlinear soil response. *Soil Dynamics and Earthquake Engineering*, *85*, 146–160. https://doi.org/10.1016/j.soildyn.2016.03.020

Chandra, J., Guéguen, P., Steidl, J. H., & Bonilla, L. F. (2015). In Situ Assessment of the G–γ Curve for Characterizing the Nonlinear Response of Soil: Application to the Garner Valley Downhole Array and the Wildlife Liquefaction Array. *Bulletin of the Seismological Society of America*, *105*(2A), 993–1010. https://doi.org/10.1785/0120140209

Derras, B., Bard, P.-Y., & Cotton, F. (2017). VS30, slope, H800 and f0: Performance of various site-condition proxies in reducing ground-motion aleatory variability and predicting nonlinear site response. *Earth, Planets and Space*, *69*. https://doi.org/10.1186/s40623-017-0718-z

EC8. (2004). *Eurocode 8 (EC8) (2004). Design of structures for earthquake resistance*. European Committee for Standardization (CEN).

EC8. (draft). *Eurocode 8 (EC8). Design of structures for earthquake resistance*. European Committee for Standardization (CEN).

Edwards, B., Michel, C., Poggi, V., & Fäh, D. (2013). Determination of Site Amplification from Regional Seismicity: Application to the Swiss National Seismic Networks. *Seismological Research Letters*, *84*, 611–621. https://doi.org/10.1785/0220120176

Fäh, D., Giardini, D., Kästli, P., Deichmann, N., Gisler, M., Schwarz-Zanetti, G., Álvarez Rubio, S., Sellami, S., Edwards, B., Goertz-Allmann, B., Bethmann, F., Woessner, J., Gassner-Stamm, G., Fritsche, S., & Eberhard, D. (2011). ECOS-09 Earthquake Catalogue of Switzerland Release 2011. *Swiss Seismological Service ETH Zürich*.

Geoprofile GmbH. (2013). *Elektrische Drucksondierungen Standortcharakterisierung SLUW* (No. 60–271).

Gisler, M., Fäh, D., & Kästli, P. (2004). Historical seismicity in Central Switzerland. *Eclogae Geologicae Helvetiae*, *97*(2), 221–236. https://doi.org/10.1007/s00015-004-1128-3

Gueguen, P., Bonilla, L., & Douglas, J. (2018). Comparison of Soil Nonlinearity ( In Situ Stress–Strain Relation and G/Gmax Reduction) Observed in Strong-Motion Databases and Modeled in Ground-Motion Prediction Equations. *Bulletin of the Seismological Society of America*, *109*. https://doi.org/10.1785/0120180169

Hegazy, Y. A., & Mayne, P. (1995). Statistical correlations between Vs and CPT data for different soil types. *Proc. Cone Penetration Testing (CPT'95)*, *2*, 173–178.

Hegazy, Y., & Mayne, P. (2006). A Global Statistical Correlation between Shear Wave Velocity and Cone Penetration Data. In *Geotechnical Special Publication* (p. 248). https://doi.org/10.1061/40861(193)31

Hobiger, M., Bard, P.-Y., Cornou, C., & Le Bihan, N. (2009). Single station determination of Rayleigh wave ellipticity by using the random decrement technique (RayDec). *Geophysical Research Letters*, *36*, L14303. https://doi.org/10.1029/2009GL038863

Hobiger, M., Bergamo, P., Imperatori, W., Panzera, F., Marrios Lontsi, A., Perron, V., Michel, C., Burjánek, J., & Fäh, D. (2021). Site Characterization of Swiss Strong-Motion Stations: The Benefit of Advanced Processing Algorithms. *Bulletin of the Seismological Society of America*, *111*(4), 1713–1739. https://doi.org/10.1785/0120200316

Hobiger, M., Imperatori, W., Bergamo, P., Lontsi, A., Michel, C., & Fäh, D. (2017). *SBUS: Buochs (NW)—Hafen* [Site Characterization Report]. Swiss Seismological Service (SED).

Iai, S., Matsunaga, Y., & Kameoka, T. (1990). *Parameter Identification for a Cyclic Mobility Model* (Report of the Port and Harbour Research Institute Vol. 29, No. 4, pp. 57–83).

Idriss, I. M., & Boulanger, R. W. (2006). Semi-empirical procedures for evaluating liquefaction potential during earthquakes. *Soil Dynamics and Earthquake Engineering*, *26*(2), 115–130. https://doi.org/10.1016/j.soildyn.2004.11.023

Ishihara, K., & Towhata, I. (1982). Dynamic response analysis of level ground based on the e®ective stress method. In *Soil Mechanics—Transient and Cyclic Loads* (G.N. Pande and O.C. Zienkiewicz Eds., pp. 133–172).

Janusz, P., Fäh, D., Perron, V., & Bonilla, L. (2021). *URBASIS deliverable: General guidelines to assess soil response in urban areas*.

Janusz, P., Perron, V., Knellwolf, C., & Fäh, D. (2022). Combining Earthquake Ground Motion and Ambient Vibration Recordings to Evaluate a Local High-Resolution Amplification Model—Insight From the Lucerne Area, Switzerland. *Frontiers in Earth Science*, *10*. https://doi.org/10.3389/feart.2022.885724

Kjartansson, E. (1979). Constant Q-wave propagation and attenuation. *Journal of Geophysical Research: Solid Earth*, *84*(B9), 4737–4748. https://doi.org/10.1029/JB084iB09p04737

Konno, K., & Ohmachi, T. (1998). Ground-motion characteristics estimated from spectral ratio between horizontal and vertical components of microtremor. *Bulletin of the Seismological Society of America*, *88*(1), 228–241. https://doi.org/10.1785/BSSA0880010228

Kramer, S. L. (1996). *Geotechnical Earthquake Engineering* (1 edition). Pearson.

Kremer, K., Wirth, S., Reusch, A., Fäh, D., Bellwald, B., Anselmetti, F., Girardclos, S., & Strasser, M. (2017). Lake-sediment based paleoseismology: Limitations and perspectives from the Swiss Alps. *Quaternary Science Reviews*, *168*, 1–18. https://doi.org/10.1016/j.quascirev.2017.04.026

Kulhawy, & Mayne. (1990). *Manual on Estimating Soil Properties for Foundation Design*.

Liao, T., Mayne, P., Tuttle, M., Schweig, E., & B. Van Arsdale, R. (2002). CPT site characterization for seismic hazards in the New Madrid seismic zone. *Soil Dynamics and Earthquake Engineering - SOIL DYNAM EARTHQUAKE ENG*, *22*, 943–950. https://doi.org/10.1016/S0267-7261(02)00118-5

Mayne, P. (2007). In-situ test calibrations for evaluating soil parameters. *Characterisation and Engineering Properties of Natural Soils*, *3*, 1601–1652. https://doi.org/10.1201/NOE0415426916.ch2

Mayne, P. (2014). Interpretation of geotechnical parameters from seismic piezocone tests. *Proceedings, 3rd International Symposium on Cone Penetration Testing (CPT14, Las Vegas)*, *102*, 47–73.

Mayne, P., & Kulhawy, F. H. (1983). K-OCR relationships in soil. *International Journal of Rock Mechanics and Mining Sciences & Geomechanics Abstracts*, *20*. https://doi.org/10.1016/0148-9062(83)91623-6

Mayne, P. W. (2006). In-Situ Test Calibrations for Evaluating Soil Parameters, Overview Paper, Characterization and Engineering Properties of Natural Soils II. *Proc. Singapore Workshop*.

Mayne, P. W., & Campanella, R. G. (2005). Versatile site characterization by seismic piezocone. *Proceedings of the 16th International Conference on Soil Mechanics and Geotechnical Engineering*, 721–724. https://doi.org/10.3233/978-1-61499-656-9-721

Mesri, G., & Abdel-Ghaffar, M. E. M. (1993). Cohesion Intercept in Effective Stress-Stability Analysis. *Journal of Geotechnical Engineering*, *119*(8), 1229–1249. https://doi.org/10.1061/(ASCE)0733-9410(1993)119:8(1229)

Michel, C., Edwards, B., Poggi, V., Burjánek, J., Roten, D., Cauzzi, C., & Fäh, D. (2014). Assessment of Site Effects in Alpine Regions through Systematic Site Characterization of Seismic Stations Assessment of Site Effects in Alpine Regions through Systematic Site Characterization of Seismic Stations. *Bulletin of the Seismological Society of America*, *104*(6), 2809–2826. https://doi.org/10.1785/0120140097

Michel, C., Poggi, V., Cauzzi, C., Burjanek, J., Roten, D., & Fäh, D. (2013). *Lucerne-Bramberg (SLUB)* [Site Characterization Report]. Swiss Seismological Service (SED).

Olsen, K. B. (2000). Site Amplification in the Los Angeles Basin from Three-Dimensional Modeling of Ground Motion. *Bulletin of the Seismological Society of America*, *90*(6B), S77–S94. https://doi.org/10.1785/0120000506

Oral, E. (2016). *Modélisation multi-dimensionnelle de la propagation des ondes sismiques dans des milieux linéaires et non-linéaires* [Phdthesis, Université Paris-Est]. https://tel.archives-ouvertes.fr/tel-01562279

Panzera, F., Bergamo, P., & Fäh, D. (2021a). Canonical Correlation Analysis Based on Site-Response Proxies to Predict Site-Specific Amplification Functions in Switzerland. *Bulletin of the Seismological Society of America*. https://doi.org/10.1785/0120200326

Panzera, F., Bergamo, P., Laurentiu, D., & Fäh, D. (2021b). *Worldwide Strong motion metadata inspection to select design-compatible waveforms for Switzerland: Preliminary results*.

Perron, V., Bergamo, P., & Fäh, D. (2022). Site amplification at high spatial resolution from combined ambient noise and earthquake recordings in Sion, Switzerland. *Seism. Res. Let. (Accepted)*.

Perron, V., Gélis, C., Froment, B., Hollender, F., Bard, P.-Y., Cultrera, G., & Cushing, E. M. (2018). Can broad-band earthquake site responses be predicted by the ambient noise spectral ratio? Insight from observations at two sedimentary basins. *Geophysical Journal International*, *215*(2), 1442–1454. https://doi.org/10.1093/gji/ggy355

Poggi, V., Edwards, B., & Fäh, D. (2011). Derivation of a Reference Shear-Wave Velocity Model from Empirical Site Amplification Derivation of a Reference Shear-Wave Velocity Model from Empirical Site Amplification. *Bulletin of the Seismological Society of America*, *101*(1), 258–274. https://doi.org/10.1785/0120100060

Poggi, V., Edwards, B., & Fäh, D. (2012a). Characterizing the Vertical-to-Horizontal Ratio of Ground Motion at Soft-Sediment Sites. *Bulletin of the Seismological Society of America*, *102*(6), 2741–2756. https://doi.org/10.1785/0120120039

Poggi, V., Fäh, D., Burjanek, J., & Giardini, D. (2012b). The use of Rayleigh-wave ellipticity for site-specific hazard assessment and microzonation: Application to the city of Lucerne, Switzerland. *Geophysical Journal International*, *188*(3), 1154–1172. https://doi.org/10.1111/j.1365-246X.2011.05305.x

Poggi, V., Michel, C., Roten, D., Burjanek, J., Cauzzi, C., & Fäh, D. (2013). *Lucerne-Werkhofstresse (SLUW)* [Site Characterization Report]. Swiss Seismological Service (SED).

Regnier, J. (2021, August). Non-Linear Soil Response At Strong Motion Observation Sites With A Focus On Borehole Array. *6th IASPEI/IAEE International Symposium: Effects of Surface Geology on Seismic Motion,*.

Robertson, P. (2009). Interpretation of cone penetration tests—A unified approach. *Canadian Geotechnical Journal*, *46*, 1337–1355. https://doi.org/10.1139/T09-065

Robertson, P., & Campanella, R. (1983). Interpretation of Cone Penetration Tests—Part I (Sand). *Canadian Geotechnical Journal*, *20*, 718–733. https://doi.org/10.1139/t83-078

Robertson, P. K. (2012). James K. Mitchell lecture: Interpretation of in-situ tests-some insights. *Geotechnical and Geophusical Site Characterization*, *1*, 3–24.

Robertson, P. K., & Cabal, K. L. (2010). Estimating soil unit weight from CPT. *2nd International Symposium on Cone Penetration Testing*.

Robertson, P. K., & Wride, C. E. (1998). Evaluating cyclic liquefaction potential using the cone penetration test. *Canadian Geotechnical Journal - CAN GEOTECH J*, *35*, 442–459.

Roten, D. (2014). *Documentation of tools for analysis of nonlinear soil behavior*.

Roten, D., Fäh, D., & Bonilla, L. (2014). Quantification of Cyclic Mobility Parameters in Liquefiable Soils from Inversion of Vertical Array Records. *Bulletin of the Seismological Society of America*, *104*, 3115–3138. https://doi.org/10.1785/0120130329

Roten, D., Fäh, D., Bonilla, L. F., Alvarez-Rubio, S., Weber, T. M., & Laue, J. (2009). Estimation of non-linear site response in a deep Alpine valley. *Geophysical Journal International*, *178*(3), 1597–1613. https://doi.org/10.1111/j.1365-246X.2009.04246.x

Sambridge, M. (1999a). Geophysical inversion with a neighbourhood algorithm—I. Searching a parameter space. *Geophysical Journal International*, *138*(2), 479–494. https://doi.org/10.1046/j.1365-246X.1999.00876.x

Sambridge, M. (1999b). Geophysical inversion with a neighbourhood algorithm—II. Appraising the ensemble. *Geophysical Journal International*, *138*(3), 727–746. https://doi.org/10.1046/j.1365-246x.1999.00900.x

Sambridge, M. (2003). *Nonlinear inversion by direct search using the Neighbourhood Algorithm*. Academic Press. https://openresearch-repository.anu.edu.au/handle/1885/62935

Schnabel, P., Lysmer, J., & Bolton Seed. (1972). *SHAKE - A Computer Program for Earthquake Response Analysis of Horizontally Layered Sites | Resolution Copper Project and Land Exchange Environmental Impact Statement*. https://www.resolutionmineeis.us/documents/schnabel-lysmer-seed-1972

Schnellmann, M., Anselmetti, F., Giardini, D., McKenzie, J., & Ward, S. (2004). Ancient Earthquakes at Lake Lucerne. *American Scientist*, *92*. https://doi.org/10.1511/2004.1.46

Schnellmann, M., Anselmetti, F. S., Giardini, D., McKenzie, J. A., & Ward, S. N. (2002). Prehistoric earthquake history revealed by lacustrine slump deposits. *Geology*, *30*(12), 1131–1134. https://doi.org/10.1130/0091-7613(2002)030<1131:PEHRBL>2.0.CO;2

SIA261. (2020). *Actions on Structures, SIA 261*. Swiss Standards, Swiss Society of Engineers and Architects.

Siegenthaler, C., Finger, W., & Kelts, K. (1987). Earthquake and seiche deposits in Lake Lucerne, Switzerland. *Eclogae Geologicae Helvetiae*, *80*(1), 241–260.

Strasser, M., Anselmetti, F. S., Fäh, D., Giardini, D., & Schnellmann, M. (2006). Magnitudes and source areas of large prehistoric northern Alpine earthquakes revealed by slope failures in lakes. *Geology*, *34*(12), 1005–1008. https://doi.org/10.1130/G22784A.1

Towhata, I., & Ishihara, K. (1985). *Modeling Soil Behavior Under Principal Axes Rotation*. 523–530.

Yoshida, N., & Iai, S. (1998). Nonlinear Site Response And Its Evaluation And Prediction. *Proc. 2nd International Symposium on the Effect of Surface Geology on Seismic Motion, Yokosuka, Japan*, 71–90.

Yu, G., Anderson, J. G., & Siddharthan, R. (1993). On the characteristics of nonlinear soil response. *Bulletin of the Seismological Society of America*, *83*(1), 218–244.

## Appendix 1

**Interpretation of CPT measurements.**



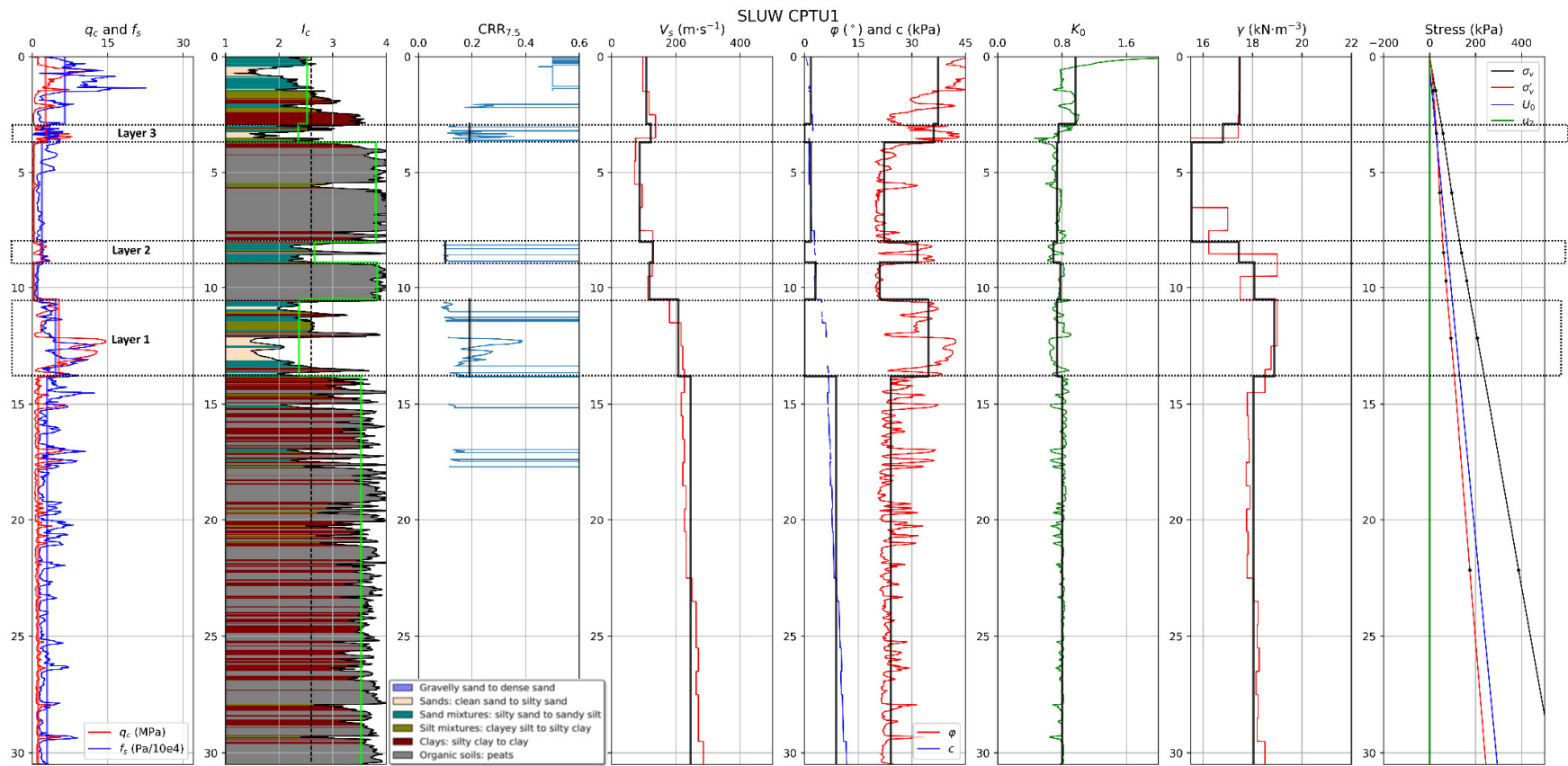*Figure 1. CPT data on the first plot and estimated soil properties for SLUW on the next plots. The explanations and empirical relations used for deriving the parameters are given in Table 1 in the report. The soil column is divided into 7 layers shown using vertical lines on each plot. Three layers marked by dashed rectangular are sandy saturated layers prone to liquefaction for which inversion for dilatancy parameters is performed.*

## Appendix 2

**Input parameters for non-linear 1D simulations.**

*Table 1. Input parameters for performing 1D simulations using NOAH. Those are parameters defining the soil column. There are additional remarks below. In addition, symbols are explained in Table 3.*

| Layer | Both linear and nonlinear layers | | | | | Nonlinear layers | | | | | Dilatancy parameters | | | | |
|---|---|---|---|---|---|---|---|---|---|---|---|---|---|---|---|
| | Depth [m] | $V_s$ [m/s] | $\rho$ [kg/m3] | Rheology | Q [-] | c [Pa] | Porosity [-] | $K_0$ [-] | $\phi$ [°] | pha [°] | $p_1$ | $p_2$ | $w_1$ | $S_1$ | $c_1$ |
| 1 | 0 | 109 | 1781 | nonlinear | 10 | 1.70E+03 | 0 | 0.97 | 37.3 | 0 | 0 | 0 | 0 | 0 | 0 |
| 2 | 0.5 | 109 | 1781 | nonlinear | 10 | 1.70E+03 | 0 | 0.97 | 37.3 | 0 | 0 | 0 | 0 | 0 | 0 |
| 3 | 2.9 | 122 | 1713 | nonlinear | 10 | 0 | 0.45 | 0.76 | 36.1 | 24.5 | 0.99 | 1.8 | 6.56 | 0.01 | 0.94 |
| 4 | 3.7 | 88 | 1584 | nonlinear | 10 | 1.70E+03 | 0 | 0.74 | 22.2 | 0 | 0 | 0 | 0 | 0 | 0 |
| 5 | 8 | 128 | 1778 | nonlinear | 10 | 0 | 0.45 | 0.69 | 31.5 | 21 | 0.96 | 1.17 | 1.87 | 0.01 | 0.65 |
| 6 | 8.9 | 118 | 1842 | nonlinear | 10 | 3.03E+03 | 0 | 0.78 | 21 | 0 | 0 | 0 | 0 | 0 | 0 |
| 7 | 10.5 | 208 | 1925 | nonlinear | 30 | 0 | 0.45 | 0.74 | 34.6 | 23.3 | 0.97 | 1.73 | 7.17 | 0.01 | 0.94 |
| 8 | 13.8 | 246 | 1838 | nonlinear | 30 | 8.80E+03 | 0 | 0.8 | 24.1 | 0 | 0 | 0 | 0 | 0 | 0 |
| 9 | 31.5 | 313 | 2000 | linear | 40 | | | | | | | | | | |
| 10 | 47.5 | 397 | 2000 | linear | 40 | | | | | | | | | | |
| 11 | 59.74 | 459 | 2000 | linear | 45 | | | | | | | | | | |
| Bedrock | 64.7 | 2333 | 2000 | | | | | | | | | | | | |

Remarks:

- Depth is depth at the top of the layer.
- P-wave velocity is calculated from $V_s$ in the code using a Poisson coefficient of 0.3 but can be defined manually for each layer.
- The best set of dilatancy parameters is given; however, we simulate wave propagation using the 30 best sets of dilatancy parameters.
- Damping (in order to control the high-frequency damping) and effective reference stress (to correct the values of the shear and rebound module as a function of depth) can be defined for each layer, here those parameters are set to 0, so no corrections are performed.
- Cohesion is defined only for clayey soils to compute the maximum shear strength.

- If the porosity is equal to 0, the excess pore pressure is not computed.
- Dilatancy parameters, as well as pha, can be ignored if excess pore pressure is not computed.

*Table 2. Input parameters for performing 1D simulations using NOAH. Those are parameters defining the computation process. More information can be found in the NOAH user manual (Bonilla, 2001).*

| | |
|---|---|
| maximum frequency [Hz] | 25 |
| points per wavelength | 20 |
| fraction of the minimum time step p0 (dt = dt * p0) | 0.6 |
| interpolation method | cosine |
| water table [m] | 0.5 |
| maximum frequency to use a lowpass filter (antialiasing) [Hz] | 15 |
| minimum frequency to use a highpass filter [Hz] | 0.1 |
| filtering | none |
| boundary condition | elastic |

*Table 3. Explanations of the symbols used in Table 1.*

| Symbol | Explanation |
|---|---|
| $V_s$ | Shear wave velocity |
| $\rho$ | density |
| Q | Quality factor |
| c | cohesion |
| $K_0$ | Coefficient of the Earth's pressure at rest |
| $\phi$ | Friction angle |
| pha | Phase transformation angle |